Received: 29 December 2020 | Revised: 10 June 2021 | Accepted: 14 June 2021

DOI: 10.1002/nme.6765

REVIEW ARTICLE

WILEY

Toward a local *maximum-entropy* material point method at finite strain within a B-free approach

Miguel Molinos[1] | **Miguel Martín Stickle**[1] | **Pedro Navas**[2] | **Ángel Yagüe**[2] | **Diego Manzanal**[2] | **Manuel Pastor**[1]

[1]Dept. of Applied Mathematics, ETSI Caminos, Canales y Puertos, Universidad Politécnica de Madrid, Madrid, Spain

[2]Dept. of Continuum Mechanics and Theory of Structures, ETSI Caminos, Canales y Puertos, Universidad Politécnica de Madrid, Madrid, Spain

Correspondence
Miguel Molinos , Dept. of Applied Mathematics, ETSI Caminos, Canales y Puertos, Universidad Politécnica de Madrid, Prof. Aranguren 3, Madrid, Spain.
Email: m.molinos@alumnos.upm.es

Funding information
H2020 Marie Skłodowska-Curie Actions, Grant/Award Number: 101007851; Ministerio de Ciencia e Innovación, Grant/Award Number: PID2019-105630GB-I00

Abstract

The material point method can be regarded as a meshfree extension of the finite element method. This fact has two interesting consequences. On the one hand, this puts a vast literature at our disposal. On the other hand, many of this inheritance has been adopted without questioning it. A clear example of it is the use of the Voigt algebra, which introduces an artificial break point between the formulation of the continuum problem and its discretized counterpart. In the authors' opinion, the use of the Voigt rules leads to a cumbersome formulation where the physical sense of the operations is obscured since the well-known algebra rules are lost. And with them, the intuition about how stresses and strains are related. To illustrate it, we will describe gently and meticulously the whole process to solve the nonlinear governing equations for isothermal finite strain elastodynamics, concluding with a compact set of expressions ready to be implemented effortless. In addition, the classic Newmark-β algorithm has been accommodated to the local *maximum-entropy* material point method framework by means of an incremental formulation.

KEYWORDS

B free, finite strain, material point method, Newmark-β, Voigt free

1 | INTRODUCTION

Large deformation problems are still considered challenging and a rich source of research in the field of computational mechanics. Classically, the finite element method (FEM) has dominated this field due to its natural robustness, moderate computational cost, and many other desirable properties. It is worth mentioning that the quality of the results in FEM simulations is highly dependent on the element aspect ratio*. This drawback takes special relevance in the large deformation regime, since mesh-based techniques are prone to suffer severe element distortion that might lead to unfinished simulations in the worst cases. To overcome this limitation, remeshing techniques have been developed within FEM. Unfortunately, these techniques are usually computationally prohibitive and its implementation is far from been trivial. Accuracy and efficiency at the finite deformation regime were the leading ideas behind the

*This aspect is controlled at the very beginning of the modelization, specifically during the meshing process.

development of mesh-free techniques. In the present days, these methods have gained a new stage of maturity and are fully established and recognized as alternatives in those scenarios where traditional mesh-dependent approaches fail. Among the wide range of proposals, the material point method (MPM) has become a robust alternative to the FEM. The MPM, originally developed in the middle of 1990s by Sulsky and coworkers,[1] benefits from a twofold description: i) a Lagrangian description where material points represent the continuum media carrying the physical information during the simulation and ii) an Eulerian description where a fixed set of nodes is considered to solve the equilibrium. Other mesh-free variational approaches share this dual description, for example, optimal transportation meshfree (OTM)[2] or element-free Galerkin method (EFGM).[3] When compared with the OTM or the EFGM, it can be observed that shape functions in the MPM are evaluated in an undeformed background set of nodes while this is not the case for the OTM or the EFGM. This strategy simplifies the computation of the shape functions and related gradients within the MPM while helps to preserves the accuracy of the mesh even when large deformations occur. The MPM algorithm can be described by the following three main steps: (i) a variational recovery process, where particle data are projected onto a set of fixed background nodes; (ii) an Eulerian step, where the balance of momentum equation is computed in the nodes; and finally (iii) a Lagrangian advection of the particles using the updated nodal information.

One of the most commonly cited shortcomings of the classical MPM approach is its inherent grid-crossing instability. It is caused by the lack of continuity in the first derivative of the shape functions between the elements. Among the different possibilities to overcome this issue, Molinos and coworkers[4,5] have proposed the use of the local maximum-entropy (LME) approximants under the MPM providing very robust results for demanding dynamic cases. The LME was originally introduced by Arroyo and Ortiz[6] as a class of convex approximation schemes, which provides a seamless transition between FEM and meshfree interpolations. The key idea behind the LME is to ensure an optimal compromise between minimizing the width of the shape function support and maximizing the entropy of the approximation. It possesses many other desirable properties for meshfree algorithms:[6] (i) they are entirely defined by the nodal set and the domain of analysis, (ii) they are also nonnegative, (iii) satisfy the partition of unity property, and (iv) provide an exact approximation of affine functions. In addition to its robustness, they are flexible enough to adapt them to a wide number of scenarios.[7] Unfortunately, this technique is computationally demanding since a minimization algorithm is required to obtain the optimal approximation for each particle. Even though, this shortcoming can be obviated by means of an efficient implementation and the use of high-performance computing techniques.

Regarding the time integration scheme, it is well known that a considerable number of current MPM researchers employs an explicit scheme[†] instead of using an implicit scheme. The reason for this choice might be the additional complexity associated with the linearization of the nonlinear equilibrium equations. This step plays a crucial role in the resolution algorithm and may be cumbersome and not trivial for complex materials if the traditional Voigt approach is considered. Conversely, the implicit solvers[9,10] might display many desirable benefits like: (i) unconditional stability, (ii) precise control of error evolution, and (iii) large load step size. Furthermore, if the linearization is done in a consistent way, the quadratic convergence of the Newton–Raphson might be achieved, and therefore, the computational cost is reduced drastically. One of the earliest papers to consider an implicit integration rule in the MPM was proposed by Guilkey and Weiss[11] who solved the nonlinear equilibrium of an hyperelastic material via the application of the trapezoidal rule along with a lumped mass approximation. Later, Sulsky and Love[12] proposed an unconditionally stable energy-momentum method taking as starting point the pioneer work of Simó and Tarnow.[13] To avoid the issues of the original formulation,[14] Sulsky and Love combined the algorithmic formula for the second Piola–Kirchhoff stress tensor $\mathbf{S}$ proposed by Gonzalez[15] and a Newton–Krylov matrix-free solver for the nonlinear system.[16] Unfortunately, the quadratic convergence of the Newton–Raphson is affected since the tangent matrix is not obtained in a consistent way. The recent developments of the implicit MPM in the finite deformation regime has been focused in solving the quasi-static equilibrium equations. First, Charlton et al.[8] introduced the implicit GIMP (iGIMP) as an implicit formulation of an elastoplastic generalized interpolation material point (GIMP) method. Iaconeta et al.[17] developed a stabilized mixed implicit formulation for nonlinear incompressible solid mechanics, and recently, Coombs et al.[18] proposed a new Lagrangian statement for large deformation elastoplasticity, the *Previously converged* formulation. In this article, we will extend the work of Guilkey and Weiss[11] to a general Newmark-β algorithm[9] formulated in an incremental fashion, that is, fluid implicit particle (FLIP) scheme.[19] These type of schemes are more convenient, since allow to preserve the complete history of stress and strain for each particle than overwriting the kinematic magnitudes

[†]This assumption was corroborated by Charlton et al.[8]

of each material point employing the particle in cell (PIC) scheme.[20] A common drawback of several of the aforementioned implicit algorithms is that they can exhibit spurious dissipative behavior in difficult situations such as collisions or other high-frequency loads. This limitation can be surmounted if algorithms like energy-momentum conserving ones[13,15,21] are consider to deal with these sort of scenarios. However, sophisticated structure of these algorithms leads to a nontrivial linearization process that is artificially difficult when algebraic manipulations are done through Voigt's rules.

As was mentioned before, when implicit algorithms are employed, a consistent linearization is required to preserve the quadratic convergence of the Newton–Raphson algorithm. A tangent elastic matrix is then obtained by the directional derivative of the residual, with respect to the displacement field. This matrix is usually computed by means of the classical[9,22] operation $\mathtt{B}^T\mathtt{DB}$, which does not require further introduction. However, a closed expression for matrix $\mathtt{D}$ may be cumbersome for certain material models or stress integration algorithms, and even more, in finite strain problems. Typically, to obtain this matrix for an arbitrary material, one finds the expression of the fourth-order tensor and, before programming it, it is converted into a matrix through the transformation rules of the Voigt algebra. Although in some materials like the St. Venant–Kirchhoff[10] model this transformation can be done easily, for other materials, with more elaborated constitutive laws, this operation is error prone. To the authors' knowledge, all the existing implicit MPM implementations are constructed following the $\mathtt{B}^T\mathtt{DB}$ setting. According to Planas et al.[23] all quantities needed to be evaluated in order to formulate and implement the FEM equations can be expressed in a natural fashion in term of vectors and second-order tensors in $\mathbb{R}^3$. Consequently, the so-called $\mathtt{B}$, and $\mathtt{D}$ matrices and Voigt vectors are not required anymore. The authors[23] highlight two main advantages: (i) the resulting expressions are much clearer, and provide a seamless transition from mathematical formulation to the implementation, which means that equations are implemented from the continuum mechanics derivation and therefore have a more natural interpretation and (ii) the compact resulting formulation allows a simple implementation which naturally exploits material symmetries to result in a very efficient code. In a later publication, Stickle et al.[24] applied the $\mathtt{B}$-free setting to the governing equations describing the consolidation process in saturated poroelastic medium with intrinsically incompressible solid and fluid phases. Recently, Antolín[25] applies this methodology for a fast assembly of stiffness matrices for laminated composites.

The original $\mathtt{B}$-free publication[23] set the advantages of leaving the less familiar Voigt's algebra in favor of a tensor-based approach in a large strain context. However, no detailed derivation of the nodal equilibrium and related linearization was presented. This last linearization step is in our understanding where the advantages of the $\mathtt{B}$-free formulation are even more dramatic in the large strain regime. Furthermore, in the aforementioned publication, no benchmark was provided to verify the performance of the $\mathtt{B}$-free approach. In order to extend Planas's work, the authors of the present research have described the complete procedure using a *Lagrangian* description for the nonlinear elastodynamic problem, providing expressions for the Ciarlet[26] Neo-Hookean material and proposing several benchmarks, see Stickle et al.[27] Some of them are also reproduced in the present research. The previously cited publications exploit the benefits of the $\mathtt{B}$-free formulation under the FEM context. In the present piece of research we fully describe the complete linearization process under the MPM framework, and provide a set of algorithms which highlight the immediate benefits of the proposal due to its natural clarity and simplicity. To the authors' knowledge the present work is the first attempt toward a $\mathtt{B}$-free approach for the MPM and could also be considered for any other variational-based meshfree technique.

The article is organized as follows: in Section 2 the strong and weak versions of the nonlinear elastodynamic problem are described. The variational problem is discretized in space by the $\mathtt{B}$-free approach and in time by an implicit Newmark scheme in Section 3 so that it can be solved by means of computational techniques. In Section 4, the goodness of the LME approximation scheme and the incremental Newmark-β in the nonlinear regime, within the $\mathtt{B}$-free formulation, are tested against analytical solution and *Lagrangian* FEM solutions. Comparison with Voigt-based solution is also included. Finally, conclusions are exposed in Section 5.

2 | THE CONTINUUM PROBLEM

The goal of this section is to present the variational formulation of the initial boundary value problem (IBVP) of nonlinear elastodynamics. The equations here described are well known, and further reading can be found in the vast bibliography available.[10,28,29] The section is organized as follows: (i) the framework description is briefly introduced in Subsection 2.1, then, (ii) the nonlinear IBVP is introduced in Subsection 2.2, and finally (iii) the variational

statement of the problem is presented in Subsection 2.3. The following convention is adopted in the present work: Three kind of subscripts or superscripts are considered: superscripts $\square^p$ denotes a particle variable, superscripts $\square^I$ is reserved for nodal variables, the subscripts $\square_n$ means time evaluation. The convention adopted for the operators is as follows: $\dot{\square}$ and $\ddot{\square}$ are considered for the first and second material time derivative, $\square \otimes \square$ means the dyadic operator, $\square \cdot \square$ and $\square : \square$ are the single and double contraction of tensor index, $\square \circ \square$ means function composition, $DIV(\square)$ denotes the divergence operator, and $GRAD(\square)$ denotes the gradient operator both in the reference configuration.

2.1 | Framework description

In order to calculate the deformation of a continuum, we must be able to mathematically describe its dynamics and its motion, also called kinematics. Specifically, we will be interested in describing the displacement, velocity, and acceleration following the motion of each individual *material point* that compose the body. This way of describing the motion is called *material* or *Lagrangian* description. To this end, consider $t \in [0, T] \subset \mathbb{R}_+$ as the time interval of interest and define $\mathcal{B}_0 \subset \mathbb{R}^{n_{dim}}$ as the *reference configuration* of a continuum body with particles $\mathbf{X} \in \mathcal{B}_0$, the so-called *material coordinates* relative to an inertial frame. As the body change its configuration[‡] with time t this leads to instantaneous or *current configuration* defined as $\mathcal{B} \subset \mathbb{R}^{n_{dim}}$. We refer to $\mathbf{x} \in \mathcal{B}$ as a point in the current configuration. The previous description of the motion is summarized in Figure 1. The set $\mathcal{B}_0$ is assumed closed, and with smooth boundary Γ_0. The reference boundary Γ_0 is introduced as a disjoint subsets such that $\Gamma_0 = \overline{\Gamma_\varphi \cup \Gamma_\sigma}$, where $\Gamma_\varphi \cap \Gamma_\sigma = \emptyset$ and the overline denoting closure. Γ_φ and Γ_σ are respectively Dirichlet and Neumann boundaries. Assume there exists a *smooth* deformation described by the *differentiable* mapping:

$$\varphi : \mathcal{B}_0 \times [0, T] \to \mathcal{B} \in \mathbb{R}^{n_{dim}} \quad \forall\, t \in [0, T], \tag{1}$$

φ is a bijective operator which relates the reference configuration $\mathcal{B}_0$ and the current configuration $\mathcal{B}$ at time t as

$$\mathbf{x} = \varphi(\mathbf{X}, t) = \mathbf{X} + \mathbf{u}(\mathbf{X}, t), \tag{2}$$

where $\mathbf{u}$ is the displacement vector. The kinematic relation expressed within Equation (2) can be articulated graphically by means of Figure 1. To describe the deformation process locally, the *deformation gradient* tensor $\mathbf{F}$ is introduced as a (two-point) tangent map between the reference configuration and the deformed configuration:

$$\mathbf{F} := \frac{\partial \varphi(\mathbf{X}, t)}{\partial X} \equiv GRAD(\varphi) = \mathbf{I} + GRAD(\mathbf{u}). \tag{3}$$

Also, the deformation gradient must satisfy the *local invertibility condition*:

$$J(\varphi) := det[\mathbf{F}] > 0, \tag{4}$$

where J represents the determinant of $\mathbf{F}$, that is, the *jacobian* of the deformation. With the previous definitions, it is possible to define the *smooth* manifold $\mathcal{Q}$ of admissible configurations:

$$\mathcal{Q} := \{\varphi : \mathcal{B}_0 \times [0, T] \to \mathbb{R}^{n_{dim}} | J(\varphi) := det[\mathbf{F}] > 0 \text{ and } \varphi|_{\Gamma_\varphi} = \overline{\varphi}\}, \tag{5}$$

where $\overline{\varphi} : \Gamma_\varphi \times [0, T] \to \mathbb{R}^{n_{dim}}$. The *material velocity* of a point is defined as $\mathbf{v}(\mathbf{X}, t) = \dot{\varphi}(\mathbf{X}, t)$ for a fixed $\mathbf{X}$, in the same way the *material acceleration* is defined as the time derivative of the material velocity $\mathbf{a}(\mathbf{X}, t) = \ddot{\varphi}(\mathbf{X}, t)$ for a fixed $\mathbf{X}$. As we can see, in the Lagrangian description, the motion is described in terms of material points. Conveniently, this way of describing the motion allows to compute easily velocity and accelerations for a given material point as we have seen before. In addition, all tensorial variables and their rates are by definition objective. Meanwhile tensorial rates expressed in deformed configuration are not necessary objective leading us to introduce intermediate mechanisms to get objective rates in the deformed configuration. In the present research we are focused in solving problems where the stress–strain

[‡]This includes displacements as a deformable body or displacements and rotations as a solid rigid.

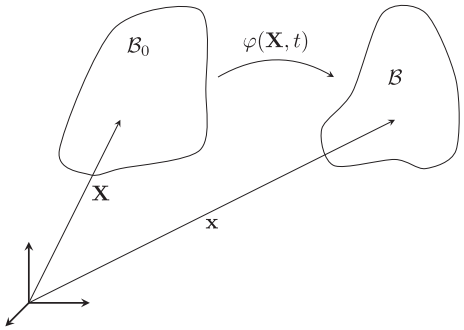

FIGURE 1 Scheme of reference and current configuration

relationship are derivable consistently from a scalar-valued *strain energy density function* W. These are the so-called *hyperelastic* materials, which also obeys frame invariance:[28]

$$W = \hat{W}(\mathbf{C}) = \hat{W}(\mathbf{F}^T\mathbf{F}) = \overline{W}(\mathbf{F}). \tag{6}$$

Being $\mathbf{C}$ the right Cauchy–Green tensor. In order to derive the large strain isothermal elastodynamic equations in the reference configuration, the *nonsymmetric* Piola–Kirchhoff stress tensor $\mathbf{P}$, which is energy conjugated to $\mathbf{F}$, is introduced as:

$$\mathbf{P} = \frac{\partial \overline{W}}{\partial \mathbf{F}} = 2\ \mathbf{F}\ \frac{\partial \hat{W}}{\partial \mathbf{C}} = \mathbf{F}\ \mathbf{S}. \tag{7}$$

The previous equation introduces the existence of the *symmetric* Piola–Kirhhoff stress tensor $\mathbf{S}$, which is energy conjugated to $\mathbf{C}$. Both magnitudes are related to the Eulerian Kirchhoff stress tensor $\boldsymbol{\tau}$ via the a contravariant pullback:

$$\mathbf{S} = \mathbf{F}^{-1}\ \mathbf{P} = \mathbf{F}^{-1}\ \boldsymbol{\tau}\ \mathbf{F}^{-T}. \tag{8}$$

As we are interested in working with symmetrical magnitudes in the reference configuration, we will consider the stress tensor $\mathbf{S}$ for the subsequent developments. Whereas the *nominal traction* is prescribed on Γ_σ as:

$$\mathbf{T}|_{\Gamma_\sigma} := \mathbf{P}\ \cdot \mathbf{N} = \mathbf{F}\mathbf{S}\ \cdot \mathbf{N} \quad \text{on} \quad \Gamma_\sigma\ \times\ [0,T] \to \mathbb{R}^{n_{dim}} \tag{9}$$

where $\mathbf{N}\ :\ \Gamma_0 \to S^2$ is the outward unit normal vector to the material boundary Γ_0. In addition, the continuum may be affected upon by an external acceleration denoted by $\mathbf{B}\ :\ \mathcal{B}_0 \times [0,T] \to \mathbb{R}^{n_{dim}}$.

2.2 | The initial boundary value problem (IBVP)

Once the framework has been clearly described in the reference configuration, the IBVP is stated in this section. First, the equilibrium is defined locally in the reference configuration as:

$$\dot{\Pi}(\mathbf{X},t) = DIV(\mathbf{F}\mathbf{S}) + \rho_0\ \mathbf{B} \quad \forall\ \mathbf{X}\ \in \mathcal{B}_0, \tag{10}$$

where Π represents the *canonical momenta* in the reference configuration. The equilibrium equation, Equation (10), is supplemented by the local relations:

$$\Pi := \rho_0\ \mathbf{v}(\mathbf{X},t), \quad \text{and} \quad \mathbf{v}(\mathbf{X},t) = \dot{\boldsymbol{\varphi}}(\mathbf{X},t) \quad \text{in} \quad \mathcal{B}_0 \times [0,T] \tag{11}$$

Finally, initial conditions are:

$$\Pi|_{t=0} = \rho_0\ \mathbf{v}(\mathbf{X},0), \quad \text{and} \quad \boldsymbol{\varphi}|_{t=0} = \boldsymbol{\varphi}(\mathbf{X},0) \quad \text{in} \quad \mathcal{B}_0. \tag{12}$$

In the absence of heat conduction, the energy function is required to satisfy the following *dissipation inequality*:[28,30]

$$\mathcal{D}^{int} := \mathcal{P}^{int} - \dot{W} \geq 0 \qquad \forall\, t \in [0, T], \tag{13}$$

being $\mathcal{D}^{int}$ the internal dissipation and $\mathcal{P}^{int}$ the stress power, which is defined as a function of the right Cauchy–Green tensor $\mathbf{C}$:

$$\mathcal{P}^{int} = \frac{1}{2}\mathbf{S} : \dot{\mathbf{C}}. \tag{14}$$

Equation (13) can be regarded as an equivalent statement of the Clausius–Duhem inequality form of the second law of thermodynamics. In this article, we will focus on those cases where internal dissipation is zero. The thermodynamic requirement expressed in Equation (13) is automatically satisfied by the Equation (7). Once the Equations (10), (11), (12), and (7) have been defined, the solution for the IBVP is closed. A natural extension of the present research is the resolution of the nonlinear viscoelasticity equation, where the internal dissipation is not zero.

2.3 | The weak form of balance of momentum

The IBVP enunciated in the previous section, Subsection 2.2, describes the motion of a continuum within a set of partial differential equations (PDEs). These equations could be solved analytically for some simple problems,[27] but have to be solved numerically for most of real problems. The approach followed by numerical techniques, such as the MPM, is first establishing a weak form, which is equivalent to the original PDEs with their initial and boundary conditions, and then solving it numerically. Following the standard arguments of variational principles, we define the following space. Let $\mathcal{W}$ denote the space of the test functions ψ associated with the admissible configurations in the manifold $\mathcal{Q}$. According to this definition, $\mathcal{W}$ is:

$$\mathcal{W} := \{\psi : \mathcal{B}_0 \to \mathbb{R}^{n_{dim}} | \psi \in \mathcal{H}^1,\ \psi|_{\Gamma_d} = \mathbf{0}\}, \tag{15}$$

where $\mathcal{H}^1$ is the first-order vector-valued Sobolev space. For the subsequent developments, Equation (10) is expressed in a more convenient residual form as:

$$\mathbf{r}(\varphi) = \dot{\Pi}(\mathbf{X}, t) + DIV(\mathbf{FS}) - \rho_0\, \mathbf{B} \qquad \forall\, \mathbf{X} \in \mathcal{B}_0. \tag{16}$$

The variational formulation of the nonlinear problem described in Section 2.2 starts premultiplying Equation (16) by the test functions ψ previously defined. Later, the resulting expression is integrated in $\mathcal{B}_0$ to obtain the integral expression of equilibrium. Hereinafter, the derived expression is integrated by parts and employing the divergence theorem and introducing the traction boundary condition (Equation 9), the following energetic *functional* (or *Lagrangian*) $\mathcal{L}(\varphi, \psi)$ is derived:

$$\mathcal{L}(\varphi, \psi) := \int_{\mathcal{B}_0} \dot{\Pi} \cdot \psi\ dV + \int_{\mathcal{B}_0} \mathbf{F}\,\mathbf{S} : GRAD(\psi)\ dV - \int_{\mathcal{B}_0} \rho_0\, \mathbf{B} \cdot \psi\ dV - \int_{\Gamma_\sigma} \mathbf{T} \cdot \psi\ dA. \tag{17}$$

Equation (17) represents the weak form equivalent to the momentum equation (Equation 16). Finally, the variational problem to solve is:

$$\text{Given a time } t \in [0, T], \text{ find } \varphi \in \mathcal{Q} \ :\ \mathcal{L}(\varphi, \psi) = 0 \quad \forall\, \psi \in \mathcal{W}.$$

$$\text{subjected to } \begin{cases} \varphi(\mathbf{X}, 0) = \varphi_0 \\ \dot{\Pi}(\mathbf{X}, 0) = \dot{\Pi}_0. \end{cases}$$

This expression defines the weak form of the problem, which will be the foundation of the MPM formulation in Section 3.

3 | THE DISCRETE PROBLEM: THE B-FREE LME-MPM FRAMEWORK

Once the continuum variational problem has been stated, it is necessary to discretize it in time and space in order to be solved by means of computer techniques. There is a whole family of variational techniques which are supported by the

TABLE 1 The α-parameters of the Newmark scheme

$\alpha_1 = \frac{1}{\beta \Delta t^2}$	$\alpha_2 = \frac{1}{\beta \Delta t}$	$\alpha_3 = \frac{1-2\beta}{2\beta}$
$\alpha_4 = \frac{\gamma}{\beta \Delta t}$	$\alpha_5 = 1 - \frac{\gamma}{\beta}$	$\alpha_6 = \left(1 - \frac{\gamma}{2\beta}\right) \Delta t$

framework derived in the previous section. The main difference between them is how spatial magnitudes are discretized. The present work focuses on the MPM technique, which relies on two different discretizations: particles and nodes. This dual approach will be further clarified across this section, which is organized as follows: first, time discretization is briefly described in Subsection 3.1; next, the spatial discretization is detailed in Subsection 3.2, continuing with the consistent linearization in Subsection 3.3 under a B-free paradigm; finally, some implementation details are considered in Subsection 3.4.

3.1 | Temporal discretization: The Newmark-β method

In this subsection, the time interval of interest $[0, T]$ is discretized into N_t time steps of length Δt through a finite collection of temporal nodes $0 < \ldots < t_n < t_{n+1} < \ldots < T$. The classical Newmark-$\beta$[31] time integration scheme is used in the present research, since it allows a comprehensive analysis of the further developments without getting lost in the details of a more sophisticated time integration scheme. Then, evaluating Equation (17) at time t_{n+1}, it is possible to solve the temporal evolution as:

$$\text{Given } \varphi_n,\ \mathbf{v}_n \text{ and } \mathbf{a}_n, \text{ find } \varphi_{n+1} \in \mathcal{Q} \ :\ \mathcal{L}(\varphi_{n+1}, \psi) = 0 \quad \forall\, \psi \in \mathcal{W}. \tag{18}$$

$$\text{subjected to } \begin{cases} \mathbf{a}_{n+1} = \alpha_1(\varphi_{n+1} - \varphi_n) - \alpha_2 \mathbf{v}_n - \alpha_3 \mathbf{a}_n \\ \mathbf{v}_{n+1} = \alpha_4(\varphi_{n+1} - \varphi_n) + \alpha_5 \mathbf{v}_n + \alpha_6 \mathbf{a}_n \end{cases} \tag{19}$$

The α-parameters are listed in Table 1 according to Wriggers.[10] On the other hand, β and γ are user parameters that might be related via the stability condition $\beta = (\gamma + 0.5)^2/4$. Details about the incremental implementation are provided in Subsection 3.4. In the current work, solutions are obtained with the trapezoidal integration rule ($\beta = 0.25$ and $\gamma = 0.5$) being unconditionally stable with second-order accuracy.[9]

3.2 | Spatial discretization: The local *max-ent* approximation as interpolation technique

Here we examine the Galerkin MPM projection of the state space $\mathcal{Q}$ onto the finite dimensional state subspace $\mathcal{Q}^h \subset \mathcal{Q}$ spanned by a convenient approximation set of interpolation functions $N^I(\mathbf{x}) : \mathcal{B} \to \mathbb{R}$. Standard Bubnov–Galerkin procedure is considered, in which the space of weighting functions $\mathcal{W}$ is projected onto a finite dimensional subspace $\mathcal{W}^h \subset \mathcal{W}$ spanned by the same functions used to approximate the configuration chart φ. The ambient space $\mathbb{R}^{n_{dim}}$ is discretized with a set of uniformly distributed spatial nodes $\mathbf{x}^I$, and a finite subset $\mathcal{A}$ of these spatial nodes is chosen such that $\mathcal{B} \subset \text{conv}\mathcal{A}$ where $\text{conv}\mathcal{A}$ is the convex hull associated with the subset $\mathcal{A}$.[6] For the sake of brevity, we will denote a node $\mathbf{x}^I$ contained in $\mathcal{A}$ as $I \in \mathcal{A}$. Spaces $\mathcal{Q}^h$ and $\mathcal{W}^h$ might be expressed as:

$$\mathcal{Q}^h := \{\varphi \in \mathcal{Q} | \varphi = \sum_{I \in \mathcal{A}} \varphi^I N^I(\mathbf{x})\}, \tag{20}$$

$$\mathcal{W}^h := \{\psi \in \mathcal{Q} | \psi = \sum_{I \in \mathcal{A}} \psi^I N^I(\mathbf{x})\}. \tag{21}$$

The spatial derivative of φ and ψ can also be computed through the support of the background set of nodes. In this article, $N^I(\mathbf{x})$ fall within the class of *convex approximation schemes*;[6] however, other approximation techniques can be applied[32-36] in the framework of the MPM. Besides, the continuum $\mathcal{B}$ is discretized with a finite set of material points[§] $\mathcal{C} \subset \mathcal{B}$. Seeking clarity for the subsequent developments, a particle $\mathbf{x}^p$ contained in $\mathcal{C}$ will be denoted as $p \in \mathcal{C}$. This set of material particles allow the definition of a configuration field φ^p, a velocity field $\mathbf{v}^p$, a mass field m^p, and stress field $\mathbf{S}^p$,

[§]Also known as particles in this article.

such that the expression ζ^p is just the evaluation $\zeta(\mathbf{x}^p)$ for each particle p. Equation (20) shows that the value of a field in a particle is performed by means of its approximation using the nodal values associated with the particle. The integrals that appear throughout the document are evaluated by means of the Riemann integral[37] applied to a finite set of points with associated volumes V^p, interpreted as quadrature weights.

$$\int_\Omega \zeta \, dV = \sum_{p \in C} \zeta^p \, V^p. \tag{22}$$

The spatial discretization described so far has been done for a generic interpolation technique. A typical pitfall of the simulations performed with the original MPM is the presence of numerical noise when particles cross the cell boundaries, commonly denoted as "cell-crossing instability." Solving this issue is the main goal[4] of the employment of the LME[6] shape functions in the MPM. The key idea behind this approximation technique is to interpret the shape function $N^I(\mathbf{x})$ as a probability. This allows to introduce two important limits: the principle of maximum-entropy (*max-ent*) statistical inference,[38] and the Delaunay triangulation which ensures the minimal width of the shape function. This approximation scheme represents an optimal compromise, in the sense of Pareto, between the *unbiased statistical inference* based on the nodal data which leads to the principle of *Maximum-Entropy* stated by Jaynes,[38] and the definition of local shape functions of *least width* the least biased shape functions. According to Arroyo and Ortiz,[6] the entropy of a discrete random variable can be defined as the uncertainty of the random variable. A measure of this uncertainty can be obtained by means of Shannon's entropy:

$$H(p^I) = -\sum_{I=1}^{N} p^I \, \log p^I, \tag{23}$$

where p^I stands for probability of the random variable outcomes, and N is the size of $\mathcal{A}$. By interpreting these probabilities as the shape functions $N^I(\mathbf{x})$ of an approximation scheme, Equation (23) can be regarded as a measure of the uncertainty of the approximation. Thus, according to Jaynes's principle of maximum entropy,[38] the least-biased approximation scheme can be given by the one that maximizes the information entropy. Thus, the control of the shape function width and its decay with distance away from the corresponding nodes is a desirable property. To reach this objective, Arroyo and Ortiz[6] propose to minimize the shape function width $U(\mathbf{x}^p, N^I)$ defined as the second moment of the shape function nodal value N^I about the position of the node $\mathbf{x}^I$. To reach a compromise between the two competing objectives, a Pareto set is considered:

$$(\mathrm{LME})_\beta \;\; \text{For fixed } \mathbf{x} \text{ minimize } f_\beta(\mathbf{x}, N^I) \equiv \hat{\beta} U(\mathbf{x}, N^I) - H(N^I)$$
$$\text{subject to } \begin{cases} N^I \geq 0, \;\; \mathrm{I} = 1, \, \dots \, , \mathrm{n} \\ \sum_{I=1}^{N} N^I = 1 \\ \sum_{I=1}^{N} N^I \mathbf{x}^I = \mathbf{x} \end{cases} .$$

The regularization or (in analogy to statistical mechanics) *thermalization* parameter, $\hat{\beta}$, between both criterion, has Pareto optimal values in the range $\hat{\beta} \in (0, \infty)$. Once the optimization problem is established, the unique solution[6] of the local *max-ent* problem LME_β is:

$$N^{I,*}(\mathbf{x}) = \frac{\exp\left[-\hat{\beta}|\mathbf{x} - \mathbf{x}^I|^2 + \lambda^* \cdot (\mathbf{x} - \mathbf{x}^I)\right]}{Z(\mathbf{x}, \lambda^*)}, \tag{24}$$

where $Z(\mathbf{x}, \lambda^*)$ is:

$$Z(\mathbf{x}, \lambda) = \sum_{I=1}^{N} \exp\left[-\hat{\beta}|\mathbf{x} - \mathbf{x}^I|^2 + \lambda \cdot (\mathbf{x} - \mathbf{x}^I)\right] \tag{25}$$

being $\lambda^*(\mathbf{x})$ the unique minimizer for the function $\log Z(\mathbf{x}, \lambda)$. The traditional way to obtain such a minimizer is applying Equation (26) to calculate small increments of $\partial\lambda$ in a Newton–Raphson solver. $\mathbf{J}$ is defined as the Hessian matrix, obtained by:

$$\mathbf{J}(\mathbf{x}, \lambda, \hat{\beta}) \equiv \frac{\partial \mathbf{r}}{\partial \lambda}, \tag{26}$$

$$\mathbf{r}(\mathbf{x}, \lambda, \hat{\beta}) \equiv \frac{\partial \log Z(\mathbf{x}, \lambda)}{\partial \lambda} = \sum_{I}^{N} p^I(\mathbf{x}, \lambda, \hat{\beta})\ (\mathbf{x} - \mathbf{x}^I). \tag{27}$$

In order to obtain easily the first derivatives of the shape function $\nabla N^{I,*}$, Arroyo and Ortiz[6] propose to consider $\hat{\beta}$ as a constant over the domain. Therefore, employing the chain rule over Equation (24), and rearranging terms, the following expression for the gradient is obtained:

$$\nabla N^{I,*} = -N_I^{I,*}\ (\mathbf{J}^*)^{-1}\ (\mathbf{x} - \mathbf{x}^I). \tag{28}$$

The regularization parameter $\hat{\beta}$ may be controlled by adjusting a dimensionless parameter, $\hat{\gamma} = \hat{\beta}h^2$, where h is defined as a measure of the nodal spacing.[6] The definition of the dimensionless parameter $\hat{\gamma}$ is independent of the number of dimensions since the thermalization parameter $\hat{\beta}$ is attached to the second-order moment definition $U(\mathbf{x}^p, N^I)$. Therefore, $\hat{\beta}$ has always $[L]^2$ units. On the other hand, the nodal distance measure adopted may depend on the number of dimensions as it is a measure of the nodal spacing.

The support of the shape functions is the entire domain conv$\mathcal{A}$, that is, the local *max-ent* shape functions are globally defined. From a practical perspective, their evaluation in the complete computational domain would result in an excessive computational cost. However, since the shape function decay as $exp(-\hat{\beta}r^2)$ with distance r to the corresponding node, its evaluation can be truncated to the set of nodes close to the particle whose basis function value is greater than a given tolerance TOL_0¶, this would ensure a reasonable range nodes to compute the shape function. Indeed, it is possible to define a circular truncation region taking the position of the particle as the center and $R_a = h\sqrt{-\log(TOL_0)/\hat{\gamma}}$ as the radius of such circle. Let us represent it as the set $\mathbb{S}^1(\mathbf{x}^p, R_a)$. This leads to a nodal subdomain $\mathcal{A}^p \subset \mathcal{A}$ which is define by the nodes $I \in \mathcal{A}$ such that also belong to $\mathbb{S}^1(\mathbf{x}^p, R_a)$. The domain of the LME shape functions proposed in the present work is conv$\mathcal{A}^p$, being convex by definition. Compared with other meshfree methods, like OTM, in the MPM the fixed background set of nodes is a discretization of the ambient space $\mathbb{R}^{n_{dim}}$, and not of the continuum body that could be nonconvex. This particular characteristic of the MPM contributes to guarantee the convexity of the LME shape function domain, avoiding the lack of the weak Kronecker-delta property, an issue widely discussed by previous authors.[6,39,40]

Some remarks clarifying some of the computational aspects regarding the LME shape function as approximation technique in the MPM are introduced for the sake of completeness.

Remarks on computational aspects

1. It is computationally expensive compared with traditional approaches such as the linear interpolation of the standard MPM or the uGIMP shape functions, since the construction of both shape functions are reduced to a mere evaluation, meanwhile for LME a Newton–Raphson is required to compute the Lagrange multiplier λ^* in each particle. However, the convergence is usually reached in few iterations.[6] In addition, the larger support of the shape functions has a negative impact in the number of the operations in each time step. By contrast, accurate results and excellent convergence properties are observed when local *max-ent* approximants are employed, see Section 4. These issues can be surmounted if high performance computing techniques are employed.[41]
2. According to Greco and Sukumar,[42] the computation of the Lagrange multipliers may blow up when the position of the particle (x^p) tends toward the boundary of the computational domain. This causes problems when imposing the Neumann boundary conditions. The simplest approach to overcome this is to employ the well-known "ghost nodes." This technique introduces additional nodes surrounding the computational domain, so that the particle will never reach the real boundary of the computational domain. Moreover, it is widely used in the context of the MPM for boundary condition imposition, see Sadeghirad et al.[33] Alternatively, by applying the l'Hôpital's rule, Greco and Sukumar[42] derive expressions to determine the derivatives of the basis functions on the boundary of a convex domain.
3. The intersection between $\mathbb{S}^1(\mathbf{x}^p, R_a)$ and conv$\mathcal{A}$ may be a task computationally expensive for large nodal sets. Therefore, a suitable alternative is here proposed. First, let us define the neighborhood of a node I as a subset of $\mathcal{A}$ which contains the surrounding nodes close to the node I, we will denote it as $\mathcal{A}^{I,n}$, where second superindex n denotes the number of "rings" of nodes close to the node I, see Figure 2(C) for details. In contrast to the heretofore implementations of the MPM search algorithm#, a closest-node algorithm is proposed instead. The target of the search algorithm

¶In this research, TOL_0 is equal to 10^{-6} according to the proposed value given by Arroyo and Ortiz.[6]
#Nodal connectivity of a given particle p is obtained doing a cell search.

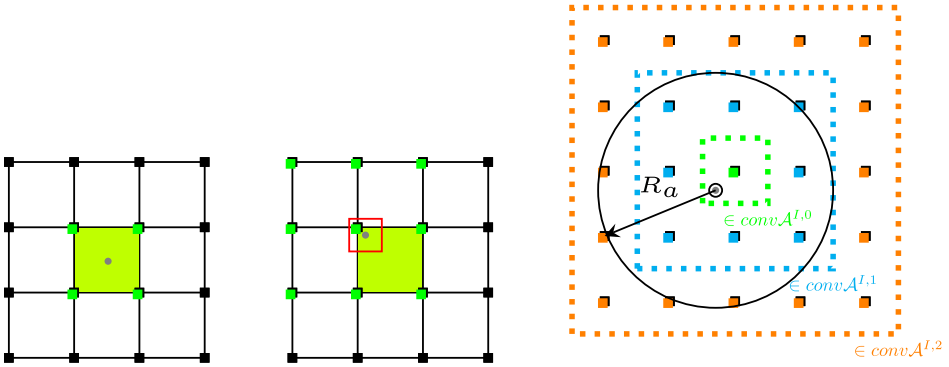

(A) Representation of the element-based connectivity of the standard-MPM.

(B) Representation of the voxel-based connectivity present in the uGIMP. As can be seen, it is an enhancement of the element-based connectivity. The red box represents the particle's voxel.

(C) Representation of the incremental rings-based approach to create nodal neighbourhood $\mathcal{A}^I$. Particle connectivity $\mathcal{A}^p$ is computed as the intersection between $\mathcal{A}^{I,n}$ and the decay circular area defined by the LME shape function evaluated in the position of the particle p, expressed as $\mathbb{S}^1(\mathbf{x}^p, R_a)$

FIGURE 2 Comparison between the connectivity definition in the standard MPM (Q4), the uniform GIMP (uGIMP), and the LME

proposed is to obtain the closest node to a given particle p. This can be done searching in the connectivity list of nodes from the last time step. Once this node I has been found, a nodal neighborhood attached to it is $\mathcal{A}^{I,n}$. In general, the size of $\mathcal{A}^{I,n}$ is much less than the size of $\mathcal{A}^I$. The election of $\mathcal{A}^{I,n}$ will depend of the value of $\hat{\beta}$ adopted for the simulation, see Figure 2(C). This reduction of the search domain simplifies the reconstruction of the nodal support for the shape function of each particle. A detailed explanation of the proposed search algorithm can be found in Algorithm 3.

4. Likewise nonpolynomial meshfree basis functions, the LME approximation scheme requires more than $d+1$ nodes to determine the values of the shape functions as well as their derivatives at any point in the convex hull of the nodal set, where d is the dimension of the problem.[6]

The advantages enumerated in this section concerning the use of *max-ent* approximants, make them a promising alternative to the existing MPM shape functions in order to mitigate problems such as cell-crossing[4] or stress instabilities in a wide range of problems. The performance of the *max-ent* approximants when dealing with the aforementioned problem under the finite strain regime is exhibited in Section 4.

3.3 | Resolution of the nonlinear system: A B-free approach

The system described by Equation (18) has a nonlinear dependence on φ_{n+1}. To face the resolution of the IBVP the approach followed in this research is the *consistent linearization* of the equilibrium equation. Since $\mathcal{L}(\varphi_{n+1}, \psi)$ is differentiable in the sense of Fréchet,[28] the best linear approximation for $\mathcal{L}(\varphi_{n+1}, \psi)$ at φ^*_{n+1} is the tangent plane $\delta\mathcal{L}(\varphi_{n+1}, \psi)$ at φ^*_{n+1}:

$$\delta\mathcal{L}(\varphi_{n+1}, \psi) = \mathcal{L}(\varphi^*_{n+1}, \psi) + D\mathcal{L}(\varphi^*_{n+1}, \psi) D\varphi_{n+1} \qquad \forall \psi \in \mathcal{W}, \tag{29}$$

being φ^*_{n+1} the last known equilibrium configuration and $D\mathcal{L}(\varphi^*_{n+1}, \psi)D\varphi_{n+1}$ the directional derivative at φ^* in the direction $D\varphi_{n+1}$ as:

$$\begin{aligned} D\mathcal{L}(\varphi^*_{n+1}, \psi)D\varphi_{n+1} &= \lim_{\epsilon\to 0} \frac{\mathcal{L}(\varphi_{n+1} + \epsilon D\varphi_{n+1},\ \psi) - \mathcal{L}(\varphi_{n+1},\ \psi)}{\epsilon} = \frac{d}{d\epsilon}\ \mathcal{L}(\varphi_{n+1} + \epsilon D\varphi_{n+1},\ \psi)\Big|_{\epsilon=0} \\ &= \int_{\mathcal{B}_0} \rho_0\ \alpha_1 D\varphi_{n+1} \cdot \psi\ dV + \int_{\mathcal{B}_0} GRAD(D\varphi_{n+1})\ \mathbf{S}_{n+1} : GRAD(\psi)\ dV \\ &\quad + \int_{\mathcal{B}_0} \mathbf{F}_{n+1}\ [\mathbb{C} : GRAD(D\varphi_{n+1})^T \mathbf{F}_{n+1}] : GRAD(\psi)\ dV. \end{aligned} \tag{30}$$

A detailed explanation of the linearization of Equation (30) can be found in Appendix A. Additionally, Equation (30) can be obtained alternatively by means of numerical approximation[43] or Newton–Krilov[16] approaches. These techniques

make possible to avoid the derivation of an analytical expression for $D\mathcal{L}(\varphi_{n+1}, \psi)$. Unfortunately, they lead to a nonconsistent tangent matrix and, therefore, the quadratic convergence of the Newton–Raphson is lost. Conversely, the numerical derivation of the tangent matrix may be convenient in cases with sophisticated stress integration rules or for a fairly general class of isotropic/nonisotropic hyperelastic materials, where the construction of the `D` matrix using the Voigt rules may be cumbersome. As was mentioned in the Abstract, the MPM relies upon many developments done in the field of the FEM. One of this is the use of the Voigt map which allow to reduce the order of fourth-order tensors to second-order tensor, and at the same time, second-order tensor to first-order tensors. These rules exploit the symmetries of some tensor structures, not necessary present in the case of nonisotropic materials, to construct the well-known derivative matrix `B` and the material elasticity matrix `D`. Both of them have been traditionally presented as convenient operators which enable the matrix formulation and FEM implementation of field theories in continuum mechanics. The simplicity in the construction of this matrix relies upon the symmetry of the some tensorial structures. A common choice in the FEM classical literature[10,29] is, once equilibrium has been linearized in the reference configuration, applying the standard contravariant push-forward operator to get the description of the motion in the deformed configuration. The late motive of this step is to recover the well-known structure of the deformed configuration and the symmetry of the associated stress measures[‖]. It is worth mentioning that the employment of the deformed configuration is done typically with the purpose of simplifying the constructions of the aforementioned structures. Due to the principle of covariance, the equilibrium can be stated in any desired configuration.[44] There is no limitation in this sense, only in the cumbersome manipulation of the Voigt structures in the reference configuration. Working in the reference configuration has some interesting properties: it is the ideal framework to linearize the nonlinear problem due to the frame invariance of $\mathcal{B}_0$; the conservation of mass is ensured by default; and any rate of a tensorial magnitude is objective by definition. Further discussion between `B`-free structure and `B`-based in the context of the FEM can be found in a previous research of the authors, see Stickle et al.[27] As will be seen in the subsequent developments, to overcome the clear limitations of the Voigt algebra the authors' bet for the use of the standard tensor calculus in pursuit of simplicity. At this stage of the development, the spatial discretization and related linearization is introduced in Equations (18) and (19) to obtain a nonlinear system of algebraic equations. Taking into account that $\forall\ \psi^I \in \mathcal{W}^h$, this leads onto the nodal evaluated counterpart of the discrete problem:

$$\text{Given } \varphi_n^I,\ \mathbf{v}_n^I,\ \text{and } \mathbf{a}_n^I, \text{ find } \varphi_{n+1}^I \in \mathcal{Q}^I \ :\ \delta\mathcal{L}(\varphi_{n+1})^I = 0, \tag{31}$$

$$\text{subject to } \begin{cases} \mathbf{a}_{n+1}^I = \alpha_1(\varphi_{n+1}^I - \varphi_n^I) - \alpha_2\mathbf{v}_n^I - \alpha_3\mathbf{a}_n^I \\ \mathbf{v}_{n+1}^I = \alpha_4(\varphi_{n+1}^I - \varphi_n^I) + \alpha_5\mathbf{v}_n^I + \alpha_6\mathbf{a}_n^I \end{cases}. \tag{32}$$

The linearized nodal equilibrium problem here defined can be regarded as a root finding problem. A typical strategy to solve it is using the Newton–Raphson method. See Appendix C for a detailed description of the implemented algorithm. Hereafter, all the terms required to obtain the linear approximation $\delta\mathcal{L}(\varphi_{n+1})^I$ will be exposed. The first structure, is the nodal discretization of the functional $\mathcal{L}(\varphi_{n+1})^I$:

$$\mathcal{L}(\varphi_{n+1})^I = \int_{\mathcal{B}_0} N(\mathbf{x})^I\ \rho_0\ N(\mathbf{x})^J dV\ \mathbf{a}_{n+1}^I + \int_{\mathcal{B}_0} \mathbf{F}_{n+1}\ \mathbf{S}_{n+1}\ :\ GRAD(N(\mathbf{x})^I)\ dV - \int_{\mathcal{B}_0} \rho_0\ \mathbf{B}_{n+1} N(\mathbf{x})^I\ dV. \tag{33}$$

Note that this expression can be implemented directly without using the matrix `B` expressed in the reference configuration[10] and the vectorized stress tensor. The implementation of Equation (33) demands some standard tensor operations, which are detailed in Algorithm 2. Hereinafter, the next step is the derivation of the directional derivative given by Equation (30) and the subsequent spatial discretization given the following expression for nodal directional derivative $D\mathcal{L}(\varphi_{n+1})^{IJ} D\varphi_{n+1}^J$:

$$\begin{aligned} D\mathcal{L}(\varphi_{n+1})^{IJ} D\varphi_{n+1}^J = \alpha_1 \int_{\mathcal{B}_0} N(\mathbf{x})^I N(\mathbf{x})^J\ \rho_0\ \mathbf{I}\ dV \cdot\ D\varphi_{n+1}^J + \int_{\mathcal{B}_0} \mathbf{S}_{n+1}\ :\ (GRAD(N(\mathbf{x}))^I\ \otimes GRAD(N(\mathbf{x}))^J)\mathbf{I}\ dV \cdot\ D\varphi_{n+1}^J \\ + \int_{\mathcal{B}_0} \mathbf{F}_{n+1}[\mathbb{C}\ :\ (\mathbf{F}_{n+1} D\varphi_{n+1}^I\ \otimes GRAD(N(\mathbf{x}))^J\ )]\ \cdot GRAD(N(\mathbf{x}))^J\ dV. \end{aligned} \tag{34}$$

[‖]Those are the Kirchhoff ($\boldsymbol{\tau}$) and Cauchy (σ) stress tensors

A complete description of the derivation for each term is detailed in the Appendix B, therefore minimal details are given in the subsequent developments. The first term in the right-hand side of Equation (34) is the contribution of inertial forces to the linearization, the coefficient α_1 arises due to the linearization of the nodal acceleration. The second term corresponds to the geometrical nonlinearity and arises after the linearization of the deformation gradient. The third term represents the contribution of the material nonlinearity to the tangent elastic matrix. The final expression of this term deserves further discussion since $D\varphi^J_{n+1}$ needs to be factored out from the expression to allow the realization of the Newton–Raphson solver for the problem stated in Equation (31). Following the classical implementation approach employed for any variational technique, Voigt rules can be introduced to factorize out $D\varphi^J_{n+1}$ which leads to a closed expression for the material tangent elastic:

$$\int_{\mathcal{B}_0} [\mathtt{B}^T \ \mathtt{D} \ \mathtt{B}]^{IJ} \, dV \, D\varphi^J_{n+1}, \tag{35}$$

where $\mathtt{D}$ is the outcome for the order reduction of the fourth-order tensor $\mathbb{C} : \square$, and $\mathtt{B}$, the linearized strain matrix at the reference configuration. Both operators have been widely described in the classical literature. The matrix $\mathtt{B}$ depends on $\mathbf{F}_{n+1}$ and $GRAD(N(\mathbf{x}))$ according to the following expression:[10]

$$\mathtt{B} = \frac{1}{2}(\mathbf{F}^{ik}_{n+1} GRAD(N(\mathbf{x}))^{I,j} + GRAD(N(\mathbf{x}))^{I,j} \mathbf{F}^{ki}_{n+1}), \tag{36}$$

which leads to a dense nontrivial matrix operator. Conversely, introducing the *material tangent density* $\mathbb{C}_{mat}\{\square, \square\}$ defined by Planas et al.[23] as:

$$\mathbb{T}\{\mathbf{v}, \mathbf{b}\} \ \delta\mathbf{a} = [\mathbb{T} : (\delta\mathbf{a} \otimes \mathbf{b})]\mathbf{v}. \tag{37}$$

for any vectors $\mathbf{v}, \mathbf{b}, \delta\mathbf{a} \in \mathbb{R}^{n_{dim}}$ and any fourth-order tensor $\mathbb{T} : \square$. Considering $\mathbf{v} = GRAD(N(\mathbf{x}))^J$, $\mathbf{b} = GRAD(N(\mathbf{x}))^I$, $\delta\mathbf{a} = \mathbf{F}_{n+1} D\varphi^I_{n+1}$, and $\mathbb{T} : \square = \mathbb{C} : \square$. Substituting these expression into Equation (34), particularizing $\mathbb{C}_{mat}\{\square, \square\}$ for a certain material and rearranging with simple algebra operations the following expression for the material tangent elastic matrix is derived:

$$\int_{\mathcal{B}_0} \mathbf{F}_{n+1} \, \mathbb{C}_{mat}\{GRAD(N(\mathbf{x}))^I, GRAD(N(\mathbf{x}))^J\} \, \mathbf{F}^T_{n+1} \, dV \, D\varphi^J_{n+1}. \tag{38}$$

Observe the mathematically clear expression of Equation (38), which respects the classical notation from differential geometry[45] on which it is built continuum mechanics theory. As we can see, this compact expression is free of Voigt's algebra structures present in Equation (35). For the special case of Neo-Hookean hyperelastic material, the *material tangent density* reads as follows:

$$\mathbb{C}_{mat}\{\mathbf{v}, \mathbf{b}\} = \Lambda J^2 (\mathbf{C}^{-1}\mathbf{v} \otimes \mathbf{C}^{-1}\mathbf{b}) \ - \left(\frac{\Lambda}{2}(J^2 - 1) - G\right)(\mathbf{C}^{-1}\mathbf{b} \cdot \mathbf{v})\mathbf{C}^{-1} - \left(\frac{\Lambda}{2}(J^2 - 1) - G\right)(\mathbf{C}^{-1}\mathbf{b} \otimes \mathbf{C}^{-1}\mathbf{v}), \tag{39}$$

where G and Λ are the well-known Lamé parameters. The derivation details of the above expression are fully detailed in Appendix B.1. Notice that, up to this point, the resolution procedure for the nonlinear equations (18) is analogous to the FEM or any other variational method; the main difference introduced by a meshfree method MPM is the evaluation of the integrals and the update of quantities. Following a $\mathtt{B}$-free approach, a transparent implementation much easier to maintain is obtained. It is probably much more efficient since assembling and operation process occurs simultaneously. The complete Newton–Raphson solver is described thorough a pseudo-algorithm 2 in Appendix C.

3.4 | The incremental Newmark-β algorithm: An updated-Lagrangian formulation

The goal of this subsection is the description of the primary steps in the proposed algorithm. Implementation details can be found in Appendix C. Given the particle data φ^p, $\mathbf{v}^p$, $\mathbf{F}^p$ from the last converged configuration, the goal is to compute

the particle data at the next time step according to the discretization techniques described in Subsections 3.1, 3.2, and 3.3. The MPM algorithm is as follows:

Nodal mask generation

In contrast to FEM, in the MPM not all the background set of nodes contain physical information since no particles may contribute to the nodes. A direct consequence is that, in MPM, only active nodes take place in the calculations. To simplify the implementation, an interesting option is to create in each time step a list with the active nodes and renumbering them. This allows to keep the nodal connectivity information, which is crucial to compute the gradients, and at the same time, to work with a reduced set of nodes.

Material point to grid projection

In the MPM the mass of each material point $m^p = \rho_0(\mathbf{x}^p)V_0^p > 0$ is constant. This ensures the mass conservation along the simulation. Using the material point masses, the *consistent* mass matrix $\mathbf{M}^{IJ}$ is defined with nodal components:

$$\mathbf{M}^{IJ} = \int_{\mathcal{B}_0} N^I \ \rho_0 \ N^J \ dV \approx \sum_{I,J \ \in \ \mathcal{A}^p} N^{Ip} \ m^p \ N^{Jp}. \tag{40}$$

According to Sulsky and Love,[12] it is convenient to consider an *effective* mass matrix $\tilde{\mathbf{M}}^{IJ}$ since there exist some material points layouts, relative to the set of nodes for which the consistent mass matrix is singular.[46] The possible singularity of the consistent mass matrix is a direct consequence of the nonoptimal quadrature rule generated, see Equation (22) in Subsection 3.2. This can be avoided if a *lumped* mass matrix $\overline{\mathbf{M}}^{IJ}$ is employed. Unfortunately it causes an $\mathcal{O}(h\Delta t^2)$ error in angular momentum conservation. Moreover, it introduces numerical damping of the order of $\mathcal{O}(h\Delta t^2)$, meanwhile energy is conserved exactly for the consistent mass matrix.[12] The use of an effective mass matrix is a compromise between numerical stability and accuracy of the solution. It is defined as the convex combination of the consistent and lumped masses:

$$\tilde{\mathbf{M}}^{IJ} := (1-\epsilon)\ \mathbf{M}^{IJ} + \epsilon\ \overline{\mathbf{M}}^{IJ}. \tag{41}$$

If $\epsilon > 0$, the effective mass matrix $\tilde{\mathbf{M}}^{IJ}$ remains positive defined. No typical values of ϵ were proposed by Sulsky and Love;[12] however, a value of $\epsilon = 0.8$ was adopted by the aforementioned authors for some benchmarks.[12] Once the effective mass matrix has been defined, nodal velocities and accelerations are calculated solving two system equivalent to a variational recovery process:

$$\tilde{\mathbf{M}}^{IJ}\ \mathbf{v}_n^J = \sum_{p \ \in \ C} N^{Ip} \ m^p \ \mathbf{v}_n^p \quad \text{and} \quad \tilde{\mathbf{M}}^{IJ}\mathbf{a}_n^J = \sum_{p \ \in \ C} N^{Ip} \ m^p \ \mathbf{a}_n^p. \tag{42}$$

The conservation properties of this step were extensively studied by Burgess et al.,[46] in addition, some concluding remarks of this step are enumerated in Love and Sulsky.[12] After getting $\mathbf{v}_n^I$, nodal values of $\varphi_{n\to n+1}^I$ are easily computed within $\Delta\varphi^I/\Delta t = \mathbf{v}_n^I$.

Updated-Lagrangian mesh dynamics

So far, the adopted formulation matches with a *Lagrangian* description. To transform the formulation into an *updated-Lagrangian* approach, the previous converged solution n is used as a support to compute the equilibrium in the reference configuration. Exploiting the group structure of φ it is possible to relate previously converged configuration $\mathcal{B}_n$ with configuration $\mathcal{B}_{n+1}$ using an intermediate mapping $\varphi_{n\to n+1}(\mathbf{x}_n, t)$ as in Figure 3:

$$\mathbf{x}_{n+1} = \varphi_{n\to n+1}(\mathbf{x}_n, t) = \varphi_{n\to n+1}(\varphi_n(\mathbf{X}, t), t) = (\varphi_{n\to n+1} \circ \varphi_n)(\mathbf{X}, t) = \varphi_{n+1}(\mathbf{X}, t). \tag{43}$$

Assuming the same fixed coordinate system for all three configurations:

$$\varphi_{n\to n+1} = \mathbf{x}_n + \Delta\varphi = \mathbf{x}_n + (\varphi_{n+1} - \varphi_n)(\mathbf{X}, t) = \mathbf{x}_n + (\varphi_{n+1} - \varphi_n)(\varphi_n^{-1}(\mathbf{x}_n, t), t) = \mathbf{x}_n + ((\varphi_{n+1} - \varphi_n) \circ \varphi_n^{-1})(\mathbf{x}_n, t). \tag{44}$$

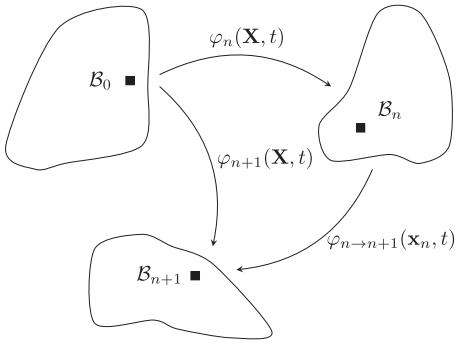

FIGURE 3 Illustration of the *updated-Lagrangian* description where $\mathcal{B}_n$ is referenced to $\mathcal{B}_{n+1}$ via the incremental deformation gradient $\Delta\mathbf{F}_{n\to n+1}$

Using the derivation chain rule is possible to get the deformation gradient at step $n+1$ as a multiplicative composition of the deformation gradient in the deformed configuration at step n and an incremental deformation gradient which takes the configuration $\mathcal{B}_n$ as reference:

$$\mathbf{F}^p_{n+1} = \frac{\partial \mathbf{x}_{n+1}}{\partial \mathbf{X}} = \frac{\partial \varphi_{n\to n+1}(\mathbf{x}_n,t)}{\partial \mathbf{X}} = \frac{\partial \varphi_{n\to n+1}(\mathbf{x}_n,t)}{\partial \mathbf{x}_n}\frac{\partial \varphi_n(\mathbf{X},t)}{\partial \mathbf{X}} = \Delta\mathbf{F}^p_{n\to n+1}\mathbf{F}^p_n. \tag{45}$$

Therefore, the incremental deformation gradient $\Delta\mathbf{F}^p_{n\to n+1}$ is defined as a tangent map which relates the body at step n with the deformed configuration at step $n+1$ as

$$\Delta\mathbf{F}^p_{n\to n+1} = \frac{\partial \varphi_{n\to n+1}}{\partial x_n}\Big|^p = \mathbf{I} + \sum_{I\,\in\,\mathcal{A}^p} \Delta\varphi^I \otimes GRAD_n(N^{Ip}), \tag{46}$$

where $GRAD_n(\square)$ is the gradient operator evaluated in the converged solution. Therefore, the incremental deformation gradient can be regarded as a deformation gradient taking the configuration in the step n as a reference configuration. Hence, the updated-Lagrangian description allows to compute the equilibrium in the reference configuration just pulling back the gradient operator from the n configuration to the reference as:

$$GRAD(\square) = (\mathbf{F}^p_n)^T\ GRAD_n(\square). \tag{47}$$

This fact has been exploited in the MPM environment by several authors.[8,12,47] On the other hand, the incremental deformation gradient $\Delta\mathbf{F}^p_{n\to n+1}$ can be applied to update other quantities such as the density. Since in the MPM the mass conservation is enforced, density and volume are updated according to Li et al.[2] as:

$$\rho^p_{n+1} = \frac{\rho^p_n}{det(\Delta\mathbf{F}^p_{n\to n+1})}, \quad \text{and} \quad V^p_{n+1} = V^p_n\ det(\Delta\mathbf{F}^p_{n\to n+1}). \tag{48}$$

Since the equilibrium is computed in the reference configuration, the current volume or density of the particle is relegated to a postprocess. Consequently, only the initial volume V^p_0 and mass m^p of the particle are required during the computations. This have a clear advantage which is the removal of a possible error source performing the operations stated in Equation (48). A final consideration of this step is that in the absence of external forces $\mathbf{F}^I_{\text{Ext},n+1} = 0$, the total mesh linear momentum is exactly conserved.

Proof. Since during Lagrangian phase the mass matrix is held constant, the proof for the conservation of the total mesh linear momentum is simple algebra:

$$\begin{aligned}\frac{\Delta\mathbf{L}^I_{n\to n+1}}{\Delta t} &= \sum_{I,J\in\mathcal{A}}\frac{1}{\Delta t}\tilde{\mathbf{M}}^{IJ}\,(\mathbf{v}^J_{n+1}-\mathbf{v}^J_n) = \sum_{I,J\in\mathcal{A}}\tilde{\mathbf{M}}^{IJ}\,\left(\frac{\gamma}{\beta\Delta t^2}\Delta\varphi^I - \frac{\gamma}{\beta\Delta t}\mathbf{v}^J_n - \left(\frac{\gamma-2\beta}{2\beta}\right)\mathbf{a}^J_n\right)\\ &= \gamma\sum_{I,J\in\mathcal{A}}\tilde{\mathbf{M}}^{IJ}\,\left(\frac{1}{\beta\Delta t^2}\Delta\varphi^I - \frac{1}{\beta\Delta t}\mathbf{v}^J_n - \left(\frac{1-2\beta}{2\beta}\right)\mathbf{a}^J_n\right) + (1-\gamma)\sum_{I,J\in\mathcal{A}}\tilde{\mathbf{M}}^{IJ}\mathbf{a}^J_n\end{aligned}$$

$$= \gamma \sum_{I,J \in \mathcal{A}} \tilde{\mathbf{M}}^{IJ} \left(\alpha_1 \Delta\varphi^I - \alpha_2 \mathbf{v}_n^J - \alpha_3 \mathbf{a}_n^J\right) + (1-\gamma) \sum_{I,J \in \mathcal{A}} \tilde{\mathbf{M}}^{IJ} \mathbf{a}_n^J$$
$$= -\gamma \sum_{I \in \mathcal{A}} \mathbf{F}_{\text{Int}}^I + (1-\gamma) \sum_{I,J \in \mathcal{A}} \tilde{\mathbf{M}}^{IJ} \mathbf{a}_n^J = 0, \tag{49}$$

which implies that $\mathbf{L}_n^I = \mathbf{L}_{n+1}^I$. ∎

Material point update

Finally, the material point information is updated using the nodal increment of the kinematic variables ($\Delta\varphi^I$, $\Delta\mathbf{v}^I$, $\Delta\mathbf{a}^I$). While $\Delta\varphi^I$ is obtained by solving the nonlinear system defined by Equation (18), the increments of nodal velocity, $\Delta\mathbf{v}^I$, and nodal acceleration, $\Delta\mathbf{a}^I$, are computed rearranging the Equation (18). Consequently, the position, velocity, and acceleration of each particle are updated via:

$$\mathbf{a}_{n+1}^p = \mathbf{a}_n^p + \sum_{I \in \mathcal{A}^p} N_n^{Ip} \, \Delta\mathbf{a}^I = \mathbf{a}_n^p + \sum_{I \in \mathcal{A}^p} N_n^{Ip} \left(\alpha_1 \Delta\varphi^I - \alpha_2 \mathbf{v}_n^I - (\alpha_3 + 1)\mathbf{a}_n^I\right), \tag{50}$$

$$\mathbf{v}_{n+1}^p = \mathbf{v}_n^p + \sum_{I \in \mathcal{A}^p} N_n^{Ip} \, \Delta\mathbf{v}^I = \mathbf{v}_n^p + \sum_{I \in \mathcal{A}^p} N_n^{Ip} \left(\alpha_4 \Delta\varphi^I + (\alpha_5 - 1)\mathbf{v}_n^I + \alpha_6 \mathbf{a}_n^I\right), \tag{51}$$

$$\mathbf{x}_{n+1}^p = \mathbf{x}_n^p + \sum_{I \in \mathcal{A}^p} N_n^{Ip} \, \Delta\varphi^I. \tag{52}$$

Using an incremental description of the motion allows to preserve energy more precisely than through a PIC scheme.[20]

Update particle nodal connectivity of each particle

With the new position of each particle, the nodal connectivity of each particle is updated using the neighborhood of the closest node. See Subsection 3.2 for a theoretical perspective of this step and the Algorithm 3 for further implementation details.

4 | NUMERICAL SIMULATIONS

This section enables the verification of the performance of the incremental Newmark-β time integration scheme as well as the local *max-ent* approximants in the finite strain regime, under the B-free framework. In the first benchmark, the longitudinal propagation of an initial discontinuity in the velocity field over an infinite homogeneous hyperelastic bar is analyzed (Subsection 4.1). The second simulation consists of the compaction, under self-weight, of a hyperelastic block (Subsection 4.2). Finally, a test proposed by Love and Sulsky[12] is depicted in order to study energy conservation properties after multiple collisions of a hyperelastic disk (see Subsection 4.3). The proposed algorithms have been implemented in our in-house software.[4] All the numerical simulations were performed with the compressible Neo-Hookean material model described in Appendix B.1.

4.1 | 1D Riemann problem at finite strain

This numerical simulation is proposed to reproduce high-frequency shocks, which in the authors' understanding is one of the most demanding benchmarks to test nonlinear elastodynamics schemes. It involves the propagation of a strong discontinuity (shock wave) in the velocity field along a 1D rectilinear bar made of a hyperelastic Neo-Hookean material with initial density $\rho_0 = 2600$ kg/m^3 and the elastic constants $\mathrm{E} = 5 \cdot 10^4$ N/m^2 and $\nu = 0.3$. For further details in this analytical solution, the interested reader is referred to the specialized literature.[48,49] A complete description of the proposed benchmark is observed in Figure 4, where material parameters, boundary conditions, initial conditions, geometry and discretization are presented. The bar has a total length of 100 m. As it is usual in the MPM, two kinds of spatial discretization are required. The first one is the spacing of the nodal background set of nodes. The bar is also discretized taking as reference the same regular mesh as for the background but with four material points per element. The total duration of the simulation is 3 ms. An special consideration must be detailed for initial conditions in this problem. Traditionally,[1] in the MPM, initial conditions are imposed in particles and later

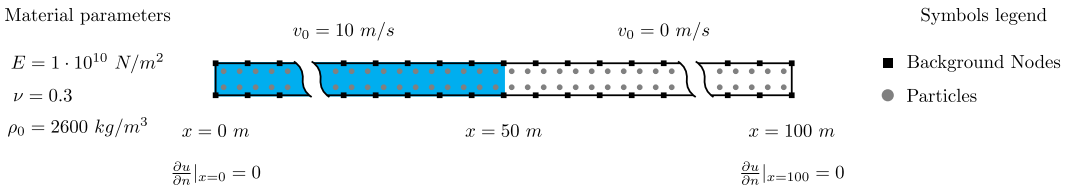

FIGURE 4 Description of the materials, boundary conditions, initial conditions, geometry and discretization of the nonlinear hyperelastic bar. The background mesh adopted for the calculations has also been plotted

transferred to the nodes as part of the standard algorithm. Nevertheless, for this research, initial conditions for velocity are imposed directly in the background set of nodes. This is a crucial decision when a nonlinear analysis is performed, and it is not relevant for a linear analysis as we can see in the propagation of a jump discontinuity[50] under the MPM framework provided by a previous research.[4] The differences between both scenarios are subtle but essential for the comprehension of why imposing initial conditions in particles instead of nodes may lead to undesired results under some special problems. In the linear case, the discontinuity is advected, not propagated, since the balance of linear momentum equations do not consider by themselves the presence of rarefaction and shock waves. In order to represent such solutions, the energy conservation equation must be introduced as an additional constraint.[51] In the case of a nonlinear problem, shocks and rarefaction waves naturally appear due to the nature of the equations. If the jump of velocities is imposed directly on the particles, when these velocities are transferred to the nodes, where real equilibrium is computed, the initial condition is degenerated into a spurious initial condition which leads to nonphysical behaviors.

4.1.1 | Sensibility of Newmark's parameters γ and β

For this example, a regular nodal spacing of 0.1 m is set, meanwhile Courant number of 1.0 controls the time step. In addition, we take $\epsilon = 0.8$ for the construction of the effective mass matrix, since offers reasonable results in terms of efficiency and stability. Figure 5 shows the final frame of the evolution of the discontinuity. This picture shows a comparison between FEM solution and MPM solution with two different spatial approximations, the standard linear interpolation Q4 and the LME approximants described in Section 3.2. About the FEM solution, a noisy solution is obtained when nondissipating configuration ($\gamma = 0.5$ and $\beta = 0.25$) is set in the Newmark solver, and as the value of γ increases, this noise is damped. However, in the MPM solution, even the solution with a nondissipating configuration of the Newmark solver has a severe damping promoted by kinetic energy dissipation during the material point to grid velocity projection. Other remarkable aspect to discuss from this figure is the presence of overshots in the solution obtained with linear interpolation, meanwhile the LME_4 solution[**] does not exhibit them. The overshot appears suddenly due to an ill-alignment between particles and the background nodes for which the consistent mass matrix is singular.[12] As was mentioned before, the nature of the equation allows the presence of shock waves, therefore, this discontinuity starts propagating. This figure highlights the importance of the spatial interpolation technique when strong discontinuities appear in the context of the large deformations.

4.1.2 | Spatial and time convergence study

In order to clarify the performance of the LME shape functions for nonlinear elasticity problems, a spatial and temporal convergence study is performed. The results of both convergence studies are reported as the L_2 norm of the error between the exact and computed velocity for the 1D Riemann problem described in Section 4.1 according to

$$\|\mathbf{e}\|_{L_2} = \left(\int_{\mathcal{B}} |\mathbf{v} - \mathbf{v}^I|^2 dx \right)^{1/2},$$

[**]The subscript four (LME_4) is referred to the value of $\hat{\gamma}$.

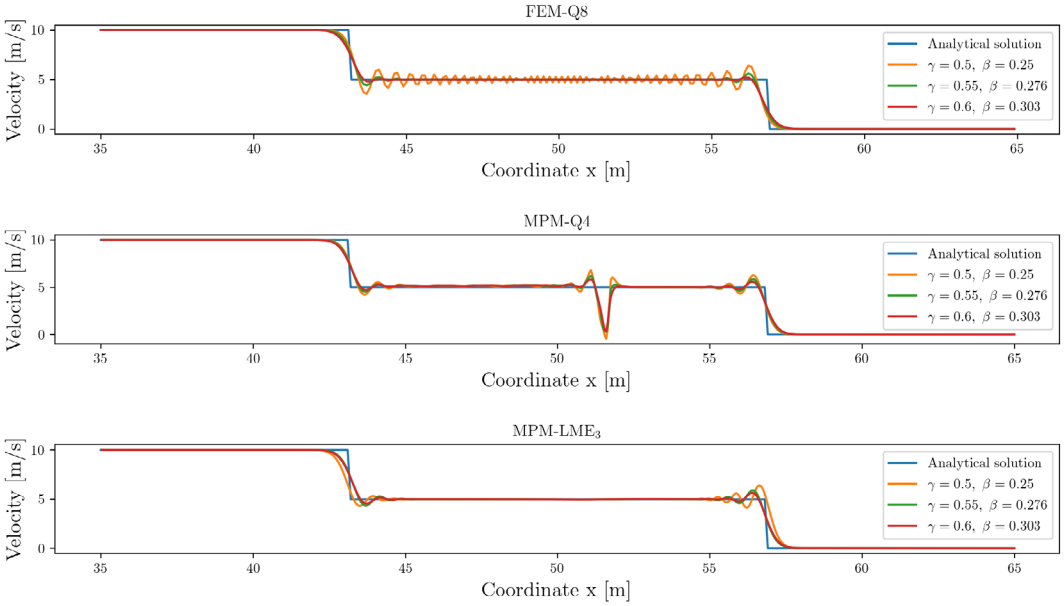

FIGURE 5 Evolution of the horizontal component of the velocity in the middle section of the bar (37–63 m) plotted at the integration points at the final step 3 ms. Three cases are analyzed, the first one is the FEM solution with an eight nodes element. The following two cases represent the MPM solution for two different spatial interpolations. The standard linear Q4 elements and the LME approximants. All configuration have been tested with three different configurations for the time integration scheme

where $\mathbf{v}^I$ is the velocity obtained by applying the algorithm, whereas $\mathbf{v}$ is the exact solution.[48,49] Results are presented in Figure 6. Regarding the spatial convergence study, five different nodal spacing where tested (0.1, 0.075, 0.05, 0.025, and 0.01), while the number of material points per element considered for each background element was four. A Courant number of one is imposed for all simulations to control the time step. Figure 6 shows how the L_2 error decreases when the nodal spacing decreases in the case of the LME solution. In the case of the standard MPM the trend is the opposite. The L_2 error increases with the mesh size. A graphical interpretation of this result is provided in the right-hand side of the Figure 6, where the velocity profile for both solutions (Q4 and LME) is plotted against the analytical solution. As we can see, the overshots observed in Figure 5 increases drastically when nodal spacing decreases. Meanwhile, the LME solution does not exhibit the presence of overshots. This result may be unexpected a priori if one considers the previous research of the authors,[4] where in both solutions the error decreases with the mesh size in a "similar" benchmark. However, in contrast with the former research, a hyperelastic constitutive model is considered, as well as the solution is calculated in the finite regime.

Concerning the temporal convergence analysis a fixed mesh size of 0.1 m is adopted for all simulations as well as the initial particle distribution per element which is fixed to four. Different values of the Courant number (1.0, 0.5, 0.1, 0.05, and 0.01) give us the time steps employed for the computation of the time convergence analysis, see Figure 7. From the interpretation of the Figure 7 it can be seen the poor behavior of the Newmark-β time integration scheme for the MPM in the finite strain regime. Although there is a minor difference between LME and Q4 solutions, this difference remains almost unchanged as the time step decreases. Therefore, the encountered discrepancy is caused by the spatial approximation technique. A natural extension of the present work should be a comparative study between different time integration schemes. The symplectic family of time integration schemes seems to be a promising alternative[12] to surmount the clear limitations of the Newmark-β.

4.2 | Compaction under self-weight

This case of study aims to test the performance of the algorithm under low-frequency loads along a prolonged period of time which are more frequent in the engineering field. It consist of the (plain strain) self-weight compaction of a square hyperelastic block of side 1 m in the dynamic regime. The initial density is $\rho_0 = 2700$ kg/m^3 and the elastic constants are $\lambda = 5 \cdot 10^4$ N/m^2, and $\mu = 3 \cdot 10^4$ N/m^2. The time step is set to $\Delta t = 0.01$ s and 500 time steps are computed. The background set of nodes consists of a cartesian grid with nodal space $\Delta x = 0.1$ m. Meanwhile, the material point

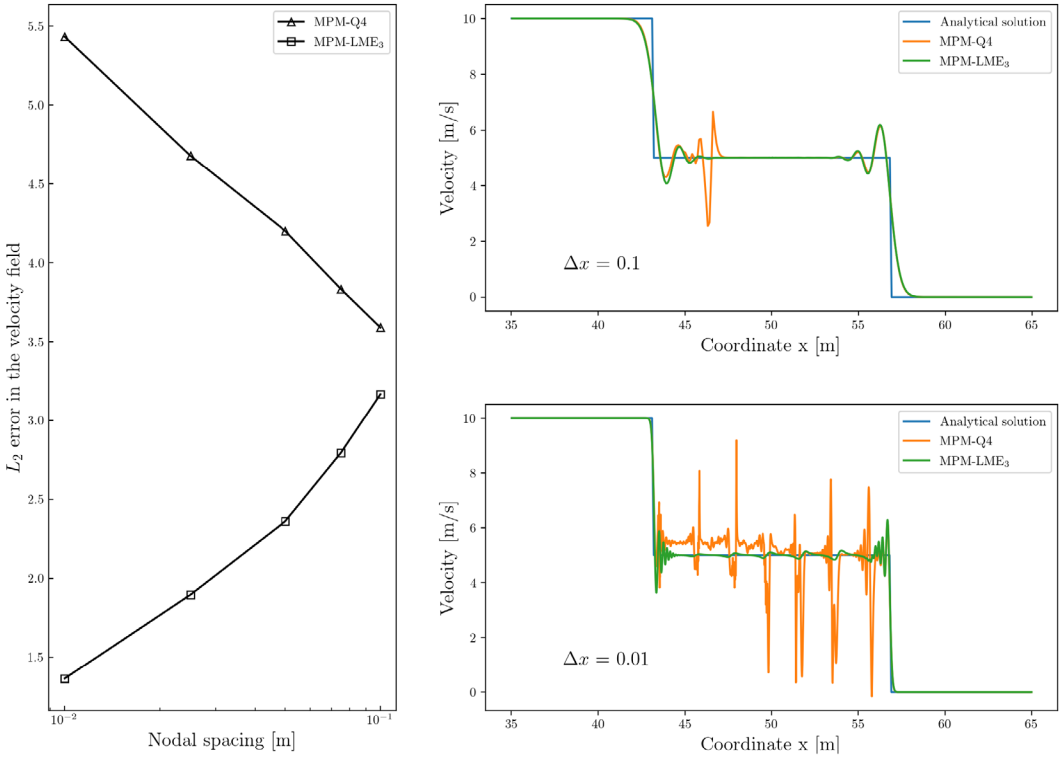

FIGURE 6 Evolution of the $\|\mathbf{e}\|_{L_2}$ error for five different mesh sizes (0.1, 0.075, 0.05, 0.025, and 0.01)

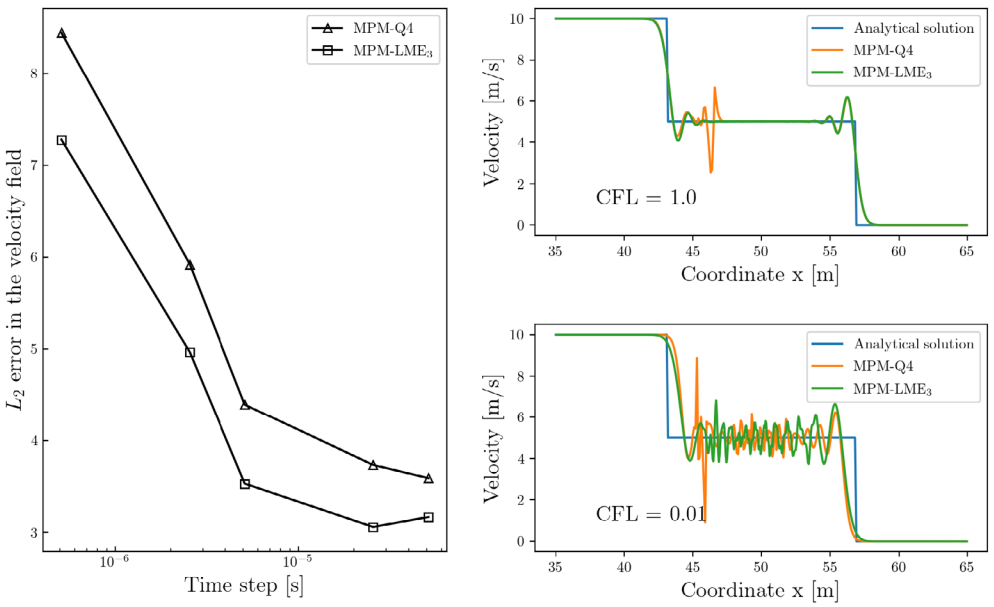

FIGURE 7 Evolution of the $\|\mathbf{e}\|_{L_2}$ error for five different time steps (5e−7, 2.5e−6, 5e−6, 2.5e−5, and 5e−5)

discretization consists of four material point per element of the background mesh. A lumped mass matrix ($\epsilon = 1.0$) has been adopted for this example. The complete description of the problem is sketched in the Figure 8, where geometry, materials and boundary conditions are presented. In addition to this figure, load curve for the gravity is presented in Figure 9(A). Figure 9(B) shows the evolution of the vertical displacement measured in a point at the middle top of the block. In this figure, FEM and MPM solutions are compared[††]. As we can see, both solution are qualitatively and

[††]Q8 elements where adopted for the FEM simulation, and LME $\hat{\gamma} = 3.0$ for the MPM simulation.

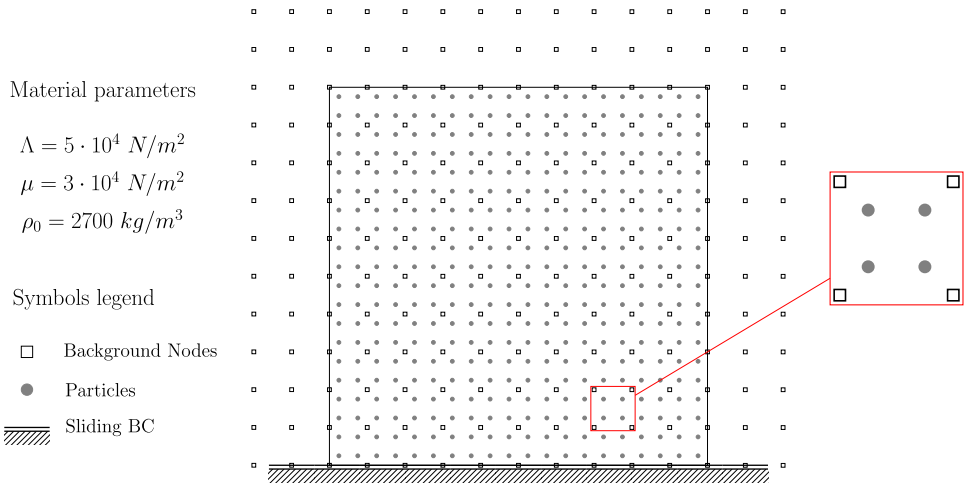

FIGURE 8 Sketch with the geometry of the block, the elastic parameters, and the initial particle layout

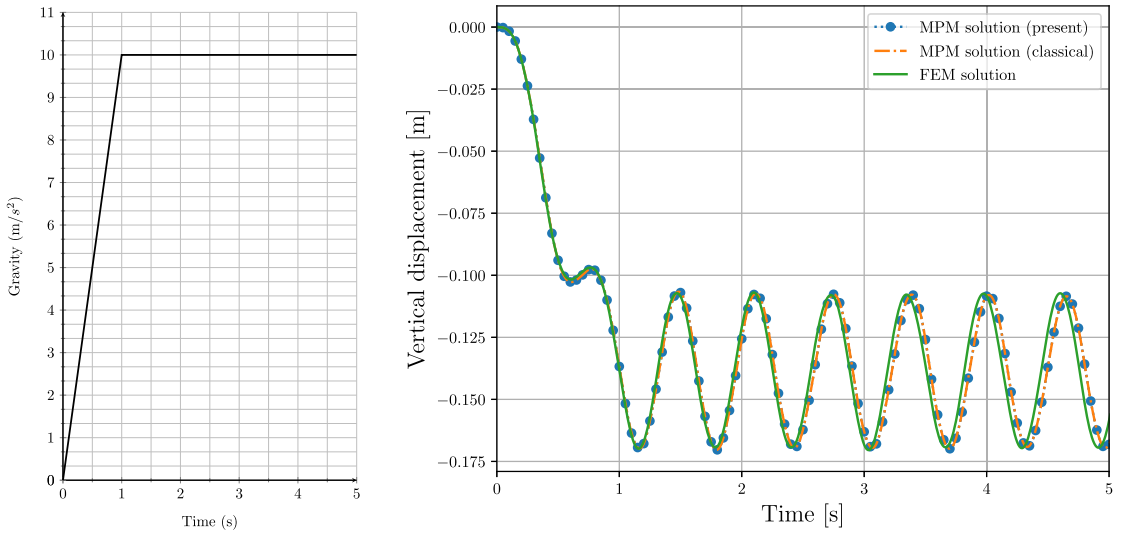

(A) Load curve for the gravity.

(B) Evolution of the vertical displacement.

FIGURE 9 Description of the gravity load and the subsequent response of the solid block

quantitatively similar. Although the nodal internal virtual work and the tangent density matrix of the proposed B-free MPM approach are, in principle, completely different from those derived in the standard Voigt-based MPM formulation, no significant differences can be appreciated between both formulations from Figure 9(B). It is worth mentioning that this assertion has been validated by the authors in Stickle et al.[27] under the FEM framework. It can be seen that both solutions tend to diverge on time, but respecting the amplitude of the oscillations. This almost negligible difference between both solutions in the time evolution is perfectly attributable to the overall difference between the two numerical techniques. However, no significant numerical damping is observed, as expected from the Newmark's parameters choice.

4.3 | Rebound of an elastic cylinder

This numerical example was taken from Love and Sulsky[12] and involves the (plain strain) impact and rebound, under plain strain conditions, of an elastic cylinder against a rigid and frictionless wall. This benchmark has no dimensions,

therefore, they are assumed to be consistent. The cylinder moves in a box of dimensions 15.0×5.0 like the sketched in Figure 10. The cylinder has an initial radius of 1.5 and its center is initially located at $(2.5, 2.5)$. The initial velocity is $(2.5, 0)$ positive in the x-axis. The initial density is $\rho_0 = 4.0$ and the elastic constant are $G = 30$ and $K = 170$. The time step is set to $\Delta t = 0.05$ and 1600 time steps are computed. The background set of nodes consist of a cartesian grid with nodal space $\Delta x = 0.5$. Two different Newmark's integration rules has been used in this example. On the one hand, the trapezoidal rule ($\gamma = 0.5,\ \beta = 0.25$) and on the other hand a damped configuration ($\gamma = 0.6,\ \beta = 0.3$). Figure 11 shows the sequence of deformed particle configuration from a simulation made with a lumped mass matrix ($\epsilon = 1.0$) matrix. The initial configuration is sketched in Figure 11(A). The cylinder translates to the right, impacts to the wall, Figure 11(B), and rebounds. After translating to the left, the cylinder impacts to the left boundary, Figure 11(C), and rebounds. Translation to the right, and another impact and rebound from the right boundary occurs, Figure 11(D). These results look like those presented in the original research.[12] Figure 12 shows the evolution of the energy for different interpolation techniques and values of the Newmark parameters γ and β. As expected, the employment of nondamping parameters for the Newmark time integration scheme ($\gamma = 0.5$ and $\beta = 0.25$) allow us to reproduce precisely the oscillation in the energy evolution due to the ringing after each impact. A careful examination of the figure shows that the use of standard linear interpolation ($Q4$ solution) introduces an extra damping, probably caused by integration errors. Moreover, more sophisticated interpolation techniques such as uGIMP and LME solutions perform this integration more precisely. It is worth mentioning that after the second impact, the LME solution exhibits and increase of the oscillations in the kinetic and mechanical energy due to the ringing of the elastic cylinder. Meanwhile, the uGIMP suffers an unphysical decrease of the oscillation analogous to the linear interpolation solution. However, despite their good results, the LME shape functions are computationally expensive, see Table 2. The large number of active nodes and the computation of Lagrange multipliers for each particle at each time step, make the use of the LME shape functions a challenging tool from the computational point of view. Therefore, for larger simulations, high-performance computing techniques should be employed in order to make this

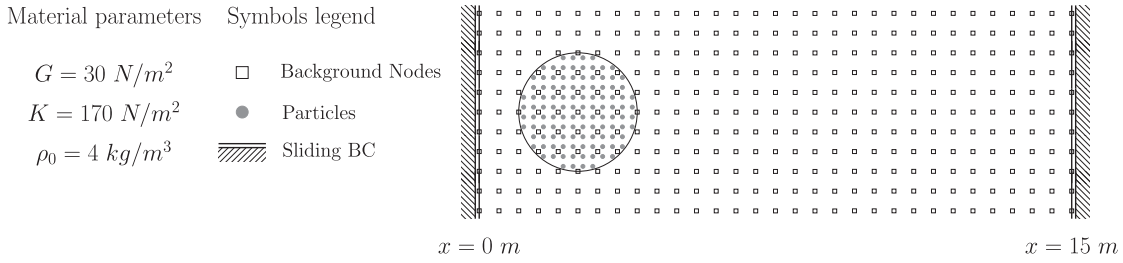

FIGURE 10 Description of the materials, boundary conditions, geometry and discretization of the nonlinear hyperelastic cylinder. Initially, the cylinder moves with a velocity $(2.5, 0)$ positive in the x-axis

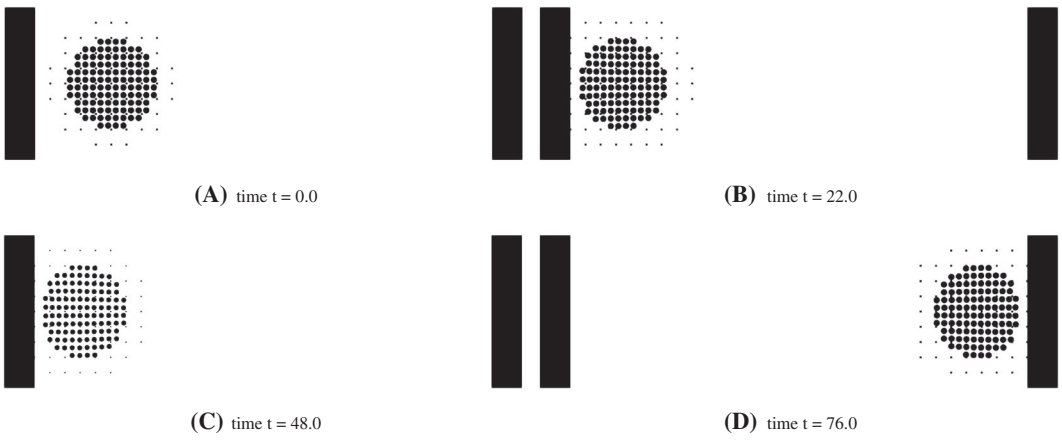

FIGURE 11 Rebound of an elastic cylinder. Sequence of deformed particle configurations for a consistent mass simulation. The red circles represents the material points and the black squares surrounding the particles are the active nodes at each time step

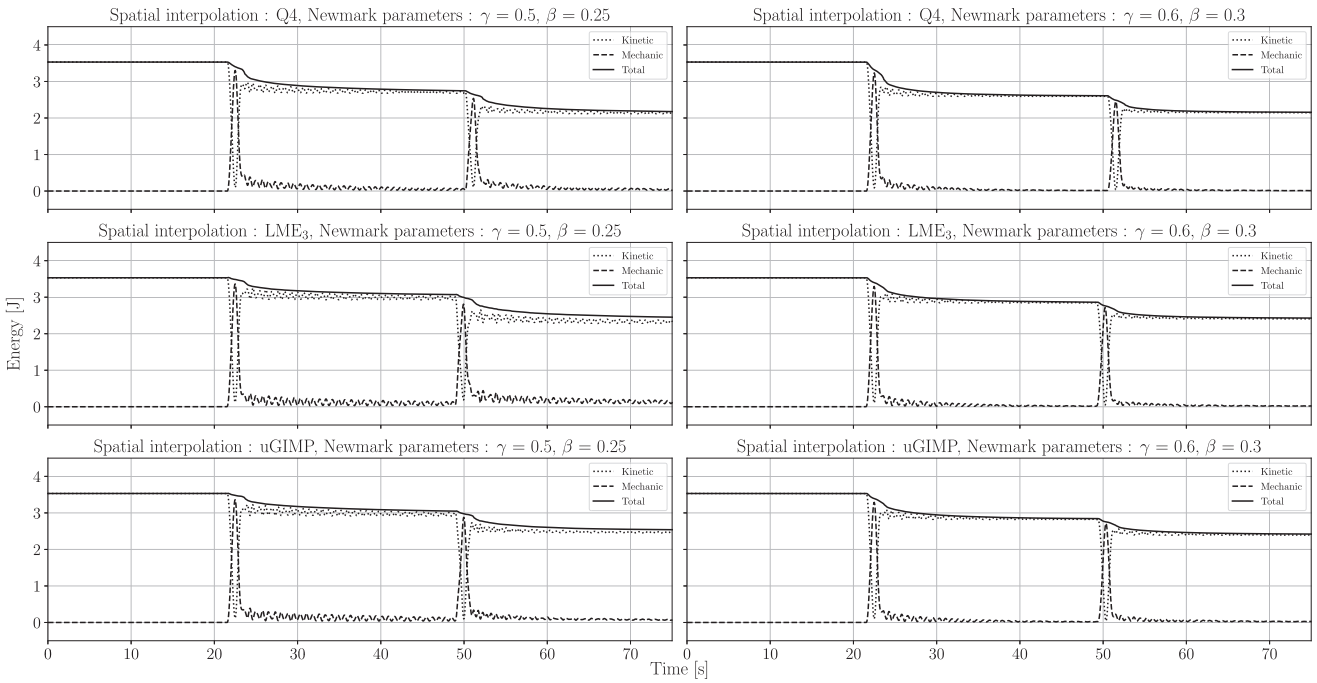

FIGURE 12 Rebound of an elastic cylinder. Evolution of total, kinetic, and internal energies for a consistent mass calculation

TABLE 2 Comparison between the three shape functions employed in terms of execution time (in seconds)

Q4	uGIMP	LME$_3$
256.32	265.31	826.01

approach computationally cheaper. On the other hand, the employment of damping parameters for the Newmark time integration scheme ($\gamma = 0.6$ and $\beta = 0.3$) has a severe impact in the conservation properties for the simulation performed with linear interpolation. Conversely, uGIMP and LME solutions seem to preserve an important amount of energy, and at the same time to reduce the oscillations as can be anticipated from this choice of parameters. As can be seen, the total amount of energy is not preserved after each impact even in the case of the trapezoidal rule. As expected, kinetic energy decreases after each collision due to the posterior ringing of the elastic cylinder. At the same time, mechanical energy should increase in the same quantity as kinetic energy decreases; however, it seems to not increase after each collision. This leads us to think that the origin of this loose of energy is due to a poor stress integration approach. These results are in line with previous observations by other researchers. See for instance the pioneering research of Dolbow and Belytschko[52] who studied the quadrature deficiency of Galerkin weak forms for meshfree methods. Recently, and under a MPM framework, Steffen et al.[53] observed a lack of convergence for the case of standard (piecewise-linear) shape functions, meanwhile, quadrature errors are drastically reduced if smoother basis functions, such as quadratic and cubic B-splines, are employed. This statement can be extended to the LME approximants case according to further research.[4,6,54] In the subsequent years, an increasing number of publications is this direction[55-57] shows that the issue of numerical integration is still an active trend of research among the meshfree community.

Other source of energy dissipation is the current time integration scheme since the same benchmark performed by the energy-momentum conserving algorithm employed by Sulsky and Love[12] does not exhibits numerical damping. Nevertheless, this issue can be surmounted in Newmark's using a small enough time step according to Kane et al.[21] They prove that Newmark can perform badly on nonlinear systems with moderate time steps as a reflection of the short time numerical stability behavior of Newmark. Regarding the numerical behavior of this approach, as occurs in Sulsky and Love,[12] convergence issues arise when a consistent matrix is employed. On the other hand, quadratic convergence is preserved if a lumped mass matrix ($\epsilon = 1.0$) is considered, see Table 3, since it is better conditioned.

TABLE 3 Convergence of the solver during the first impact ($t = 22.0$)

Iteration number	Absolute error	Relative error
0	1.3336e+02	1.0000e+00
1	2.0710e−02	1.5529e−04
2	2.4353e−08	1.8260e−10

Note: This results were obtained using a lumped mass matrix ($\epsilon = 1.0$).

5 | CONCLUSIONS

The present research advocates for a change in the current large strain MPM paradigm within the employment of a tensor-based implementation which is simpler and free of the artificial Voigt algebra. This approach seems to be well suited for variational meshfree approaches such as the MPM. Throughout this research, we have shown that, following the B-free philosophy, it is possible to set a robust numerical framework to solve a continuum problem at large strains where the time and space discretization process, as well as the implementation can be performed without leaving the standard $\mathbb{R}^3$ tensor algebra. Moreover, since the B-free approach is actually a component-free approach where only intrinsic operations are required the extension of the proposed algorithm from a Cartesian coordinate system to a general curvilinear coordinate system or even from 2D to 3D is straightforward when compared with the use of Voigt's Algebra, allowing for a smooth transition from the handwriting equations to the implementation. The results presented in this research shows that LME approximants exhibit remarkable properties in terms of convergence and smoothing the presence of spurious overshots without introducing excessive damping. What is more, the use of these special interpolation techniques seems to be more crucial for large deformation scenarios where the grid-crossing error present in standard linear interpolation cannot be tolerated. At the same time, the interpretation of the LME approximant here proposed circumvent the presence of nonconvex nodal domains, safeguarding the weak Kronecker-delta property. Therefore, the combination between these two techniques seems to be a promising and robust alternative to the existing MPM approaches. On the other hand, the Newmark-β method has been implemented under an incremental configuration and validated with satisfactory results against challenging cases exhibiting good accuracy.

In future research, more elaborated and mathematically challenging formulations will be sought to reinforce the appropriateness of this paradigm. Some of them are (i) the extension of this approach to include viscoelasticity sources. A first approach to consider this situation is the implementation of the viscoelastic Kelvin model,[58] or introducing a generalized relaxation model.[28] (ii) The formulation of soil–water coupled problems adapting the previous work of the authors[59] to a B-free Lagrangian setting. (iii) Finally, revisiting some sophisticated time integration schemes[12] to provide an analytical expression to the tangent elastic matrix.

ACKNOWLEDGMENTS

This research has been financially supported by: the PLAND project from the Ministerio de Ciencia e Innovación, under Grant No. PID2019-105630GB-I00, and the DISCO2-STORE project from the European Commission-H2020 MSCA-RISE 2020, under Grant No. 101007851. Additionally, the first author really appreciate the Fundación Entrecanales Ibarra for his predoctoral fellowship.

CONFLICT OF INTEREST

The authors declare no potential conflict of interests.

AUTHOR CONTRIBUTIONS

Conceptualization and mathematical methodology, Miguel Molinos Pérez and Miguel Martín Stickle. Implementation, Miguel Molinos Pérez and Pedro Navas. Validation, Ángel Yagüe and Diego Manzanal. Supervision, Manuel Pastor. Meanwhile project administration and funding acquisition belongs to Manuel Pastor and Diego Manzanal. All authors have contributed to the writing and original draft preparation and they read and agreed to the published version of the manuscript.

DATA AVAILABILITY STATEMENT

The data that support the findings of this study are available from the corresponding author upon reasonable request.

NOMENCLATURE

$D\varphi$	directional derivative of the configuration mapping
J	Jacobian of the deformation gradient tensor
W	strain energy function
$DIV(\square)$	divergence operator in the reference configuration
$GRAD(\square)$	gradient operator in the reference configuration $\mathcal{B}_0$
$GRAD_n(\square)$	gradient operator in the reference configuration $\mathcal{B}_n$
Γ_0	reference boundary
Γ_σ	natural or Neumann boundary conditions over Γ_0
Γ_φ	essential or Dirichlet boundary conditions over Γ_0
Π	Canonical momenta
$\ddot{\square}$	second material time derivative
$\dot{\square}$	first material time derivative
$\mathbb{C} : \square$	constitutive fourth-order tensor
$\mathbb{C}_{mat} : \{\square, \square\}$	material tangent density operator
$\mathbf{X}$	material coordinates
$\mathbf{x}$	spatial coordinates
$\mathcal{A}^p$	list of nodes for each particle
$\mathcal{B}_0$	reference configuration
$\mathcal{B}$	deformed configuration
$\mathcal{D}^{int}$	internal dissipation
$\mathcal{H}^1$	vector Sobolev space of degree 1
$\mathcal{P}^{int}$	stress power
$\mathcal{Q}$	smooth manifold of admissible configurations
$\mathcal{W}$	space of the test functions ψ
$\mathtt{B}$	standard strain-displacement matrix
ψ	test functions
σ	Cauchy stress tensor
$\square \cdot \square$	single contraction operator
$\square \circ \square$	function composition
$\square : \square$	double contraction operator
$\square \otimes \square$	dyadic operator
$\square^I$	nodal variable
$\square^p$	particle variable
$\square_n$	time evaluation of a variable at $t = n$
$\mathbf{C}$	right Cauchy–Green strain tensor, $\mathbf{C} := \mathbf{F}^T\mathbf{F}$
$\mathbf{F}$	deformation gradient tensor
$\mathbf{P}$	first Piola–Kirchhoff stress tensor
$\mathbf{S}$	second Piola–Kirchhoff stress tensor
$\boldsymbol{\tau}$	Kirchhoff stress tensor $\tau = J\sigma$
$\mathbf{u}$	displacement field
φ	configuration mapping
$\hat{\beta}$	regularization or thermalization parameter of the LME_β Pareto set

ORCID

Miguel Molinos https://orcid.org/0000-0002-5073-4796
Miguel Martín Stickle https://orcid.org/0000-0001-7591-418X
Pedro Navas https://orcid.org/0000-0002-0482-378X
Ángel Yagüe https://orcid.org/0000-0002-3290-9433
Diego Manzanal https://orcid.org/0000-0002-6087-3255
Manuel Pastor https://orcid.org/0000-0001-8080-0013

REFERENCES

1. Sulsky DL, Schreyer H, Chen Z. A particle method for history-dependent materials. *Comput Methods Appl Mech Eng*. 1994;118(1):179-196. https://doi.org/10.1016/0045-7825(94)90112-0
2. Li B, Habbal F, Ortiz M. Optimal transportation meshfree approximation schemes for fluid and plastic flows. *Int J Numer Methods Eng*. 2010;83(12):1541-1579. https://doi.org/10.1002/nme.2869
3. Lu Y, Belytschko T, Gu L. A new implementation of the element free Galerkin method. *Comput Methods Appl Mech Eng*. 1994;113(3):397-414. https://doi.org/10.1016/0045-7825(94)90056-6
4. Molinos M, Navas P, Pastor M, Martín SM. On the dynamic assessment of the local-maximum entropy material point method through an explicit predictor-corrector scheme. *Comput Methods Appl Mech Eng*. 2021;374:113512. https://doi.org/10.1016/j.cma.2020.113512
5. Molinos M, Navas P, Manzanal D, Pastor M. Local maximum entropy material point method applied to quasi-brittle fracture. *Eng Fract Mech*. 2021;241:107394. https://doi.org/10.1016/j.engfracmech.2020.107394
6. Arroyo M, Ortiz M. Local maximum-entropy approximation schemes: a seamless bridge between finite elements and meshfree methods. *Int J Numer Methods Eng*. 2006;65(13):2167–2202. https://doi.org/10.1002/nme.1534
7. Kumar S, Kochmann DM. Enhanced local maximum-entropy approximation for stable meshfree simulations. *Comput Methods Appl Mech Eng*. 2019;344:858–886. https://doi.org/10.1016/j.cma.2018.10.030
8. Charlton TJ, Coombs WM, Augarde CE. iGIMP: an implicit generalised interpolation material point method for large deformations. *Comput Struct*. 2017;190:108-125. https://doi.org/10.1016/j.compstruc.2017.05.004
9. Hughes TJR. *The Finite Element Method: Linear Static and Dynamic Finite Element Analysis*. Mineola, NY: Dover Publications; 2000.
10. Wriggers P. *Nonlinear Finite Element Methods*. 1st ed. Berlin/Heidelberg, Germany: Springer-Verlag; 2008.
11. Guilkey J, Weiss J. Implicit time integration for the material point method: quantitative and algorithmic comparisons with the finite element method. *Int J Numer Methods Eng*. 2003;57:1323-1338. https://doi.org/10.1002/nme.729
12. Love E, Sulsky D. An unconditionally stable, energy–momentum consistent implementation of the material-point method. *Comput Methods Appl Mech Eng*. 2006;195(33):3903-3925. https://doi.org/10.1016/j.cma.2005.06.027
13. Simó JC, Tarnow N. The discrete energy-momentum method. Conserving algorithms for nonlinear elastodynamics. *Zeitschrift für angewandte Mathematik und Physik ZAMP*. 1992;43:757–792. https://doi.org/10.1007/BF00913408
14. Laursen T, Meng X. A new solution procedure for application of energy-conserving algorithms to general constitutive models in nonlinear elastodynamics. *Comput Methods Appl Mech Eng*. 2001;190(46):6309-6322. https://doi.org/10.1016/S0045-7825(01)00257-2
15. Gonzalez O. Exact energy and momentum conserving algorithms for general models in nonlinear elasticity. *Comput Methods Appl Mech Eng*. 2000;190(13):1763-1783. https://doi.org/10.1016/S0045-7825(00)00189-4
16. Sulsky D, Kaul A. Implicit dynamics in the material-point method. *Comput Methods Appl Mech Eng*. 2004;193(12):1137-1170. https://doi.org/10.1016/j.cma.2003.12.011
17. Iaconeta I, Larese A, Rossi R, Oñate E. A stabilized mixed implicit material point method for non-linear incompressible solid mechanics. *Comput Mech*. 2018;63:1243-1260. https://doi.org/10.1007/s00466-018-1647-9
18. Coombs WM, Augarde CE, Brennan AJ, et al. On Lagrangian mechanics and the implicit material point method for large deformation elasto-plasticity. *Comput Methods Appl Mech Eng*. 2020;358:112622. https://doi.org/10.1016/j.cma.2019.112622
19. Brackbill J, Kothe D, Ruppel H. Flip: a low-dissipation, particle-in-cell method for fluid flow. *Comput Phys Commun*. 1988;48(1):25-38. https://doi.org/10.1016/0010-4655(88)90020-3
20. Harlow FH, Evans MW. *A Machine Calculation Method for Hydrodynamic Problems*. California: Los Alamos Scientific Laboratory of the University of California; 1956.
21. Kane C, Marsden JE, Ortiz M, West M. Variational integrators and the Newmark algorithm for conservative and dissipative mechanical systems. *Int J Numer Methods Eng*. 2000;49(10):1295-1325. https://doi.org/10.1002/1097-0207(20001210)49:10<1295::AID-NME993>3.0.CO;2-W
22. Zienkiewicz OC, Taylor RL, Zhu JZ. *The Finite Element Method: Its Basis and Fundamentals*. 6th ed. Oxford, United Kingdom: Butterworth-Heinemann; 2005.
23. Planas J, Romero I, Sancho J. B free. *Comput Methods Appl Mech Eng*. 2012;217-220:226-235. https://doi.org/10.1016/j.cma.2012.01.019
24. Stickle M, Yague A, Pastor M. B free finite element approach for saturated porous media: consolidation. *Math Probl Eng*. 2016;2016:1–12. https://doi.org/10.1155/2016/4256079
25. Antolin P. Fast assembly of Galerkin matrices for 3D solid laminated composites using finite element and isogeometric discretizations. *Comput Mech*. 2020;65(1):135-148. https://doi.org/10.1007/s00466-019-01756-6
26. Ciarlet PG. Chapter 4 Hyperelasticity. In: Ciarlet PG, ed. *Mathematical Elasticity Volume I: Three-Dimensional Elasticity. Volume 20 of Studies in Mathematics and Its Applications*. North Holland: Elsevier; 1988:137-198.
27. Stickle M, Molinos M, Navas P, et al. B free Lagrangian formulation for large strain elastodynamics. *Comput Mech*.
28. Simó JC, Hughes TJR. *Computational Inelasticity*. New York, NY: Springer-Verlag; 1998.
29. Bonet J, Wood RD. *Nonlinear Continuum Mechanics for Finite Element Analysis*. Cambridge, MA: Cambridge University Press; 2008.
30. Antman SS. *Nonlinear Problems of Elasticity*. 2nd ed. Berlin/Heidelberg, Germany: Springer-Verlag; 2005.
31. Newmark NM. A method of computation for structural dynamics. *J Eng Mech Div*. 1959;85:67-94.
32. Bardenhagen SGSG, Kober EM. The generalized interpolation material point method. *CMES - Comput Model Eng Sci*. 2004;5(6):477-495.
33. Sadeghirad A, Brannon RM, Burghardt J. A convected particle domain interpolation technique to extend applicability of the material point method for problems involving massive deformations. *Int J Numer Methods Eng*. 2011;86(12):1435-1456. https://doi.org/10.1002/nme.3110

34. Zhang DZ, Ma X, Giguere PT. Material point method enhanced by modified gradient of shape function. *J Comput Phys*. 2011;230(16):6379-6398. https://doi.org/10.1016/J.JCP.2011.04.032
35. Tielen R, Wobbes E, Möller M, Beuth L. A high order material point method. *Proc Eng*. 2017;175:265-272. Proceedings of the 1st International Conference on the Material Point Method (MPM 2017). https://doi.org/10.1016/j.proeng.2017.01.022
36. de Koster P, Tielen R, Wobbes E, Möller M. Extension of B-spline material point method for unstructured triangular grids using Powell–Sabin splines. *Comput Part Mech*. 2020. https://doi.org/10.1007/s40571-020-00328-3
37. Riemann B. Über die Darstellbarkeit einer Function durch eine trigonometrische Reihe. *Abhandlungen der Königlichen Gesellschaft der Wissenschaften zu Göttingen*. 1854;13:87-138. https://doi.org/10.1016/j.cma.2017.09.022
38. Jaynes E. Information theory and statistical mechanics. *Phys Rev*. 1957;106(4):620-630. https://doi.org/10.1103/PhysRev.106.620
39. Rosolen A, Arroyo M. Blending isogeometric analysis and local maximum entropy meshfree approximants. *Comput Methods Appl Mech Eng*. 2013;264:95-107. https://doi.org/10.1016/j.cma.2013.05.015
40. Greco F, Filice L, Peco C, Arroyo M. A stabilized formulation with maximum entropy meshfree approximants for viscoplastic flow simulation in metal forming. *Int J Mater Form*. 2015;8:341-353. https://doi.org/10.1007/s12289-014-1167-x
41. Li B, Stalzer M, Ortiz M. A massively parallel implementation of the optimal transportation meshfree method for explicit solid dynamics. *Int J Numer Methods Eng*. 2014;100(1):40-61. https://doi.org/10.1002/nme.4710
42. Greco F, Sukumar N. Derivatives of maximum-entropy basis functions on the boundary: theory and computations. *Int J Numer Methods Eng*. 2013;94(12):1123-1149. https://doi.org/10.1002/nme.4492
43. Wriggers P, Simo JC. A general procedure for the direct computation of turning and bifurcation points. *Int J Numer Methods Eng*. 1990;30(1):155-176. https://doi.org/10.1002/nme.1620300110
44. Simo JC, Marsden JE. Stress tensors, Riemannian metrics and the alternative descriptions in elasticity. In: Ciarlet PG, Roseau M, eds. *Trends and Applications of Pure Mathematics to Mechanics*. Berlin/Heidelberg, Germany: University of California Berkeley, Springer; 1984:369-383.
45. Abraham R, Marsden J, Ratiu T. *Manifolds, Tensor Analysis, and Applications*. Applied Mathematical Sciences. Berlin/Heidelberg, Germany: Springer; 1988.
46. Burgess D, Sulsky D, Brackbill J. Mass matrix formulation of the FLIP particle-in-cell method. *J Comput Phys*. 1992;103(1):1-15. https://doi.org/10.1016/0021-9991(92)90323-Q
47. Coombs WM, Charlton TJ, Cortis M, Augarde CE. Overcoming volumetric locking in material point methods. *Comput Methods Appl Mech Eng*. 2018;333:1-21. https://doi.org/10.1016/j.cma.2018.01.010
48. Godlewski E, Raviart PA. *Numerical Approximation of Hyperbolic Systems of Conservation Laws*. Applied Mathematical Sciences. Berlin/Heidelberg, Germany: Springer; 1996.
49. Dafermos CM. *Hyperbolic Conservation Laws in Continuum Physics*. Grundlehren der mathematischen Wissenschaften. Berlin/Heidelberg, Germany: Springer; 2009.
50. Dyka C, Ingel R. An approach for tension instability in smoothed particle hydrodynamics (SPH). *Comput Struct*. 1995;57(4):573-580. https://doi.org/10.1016/0045-7949(95)00059-P
51. Zhang X, Chen Z, Liu Y. *The Material Point Method: A Continuum-Based Particle Method for Extreme Loading Cases*. North Holland: Elsevier; 2016.
52. Dolbow J, Belytschko T. Numerical integration of the Galerkin weak form in meshfree methods. *Comput Mech*. 1999;23:219-230. https://doi.org/10.1007/s004660050403
53. Steffen M, Kirby RM, Berzins M. Analysis and reduction of quadrature errors in the material point method (MPM). *Int J Numer Methods Eng*. 2008;76(6):922-948. https://doi.org/10.1002/nme.2360
54. González D, Cueto E, Doblaré M. A higher order method based on local maximum entropy approximation. *Int J Numer Methods Eng*. 2010;83(6):741-764. https://doi.org/10.1002/nme.2855
55. Sulsky D, Gong M. Improving the material-point method. *Innovative Numerical Approaches for Multi-Field and Multi-Scale Problems*. Cham, Switzerland: Springer; 2016.
56. Wobbes E, Möller M, Galavi V, Vuik C. Conservative Taylor least squares reconstruction with application to material point methods. *Int J Numer Methods Eng*. 2019;117(3):271-290. https://doi.org/10.1002/nme.5956
57. Tran QA, Sołowski W, Berzins M, Guilkey J. A convected particle least square interpolation material point method. *Int J Numer Methods Eng*. 2020;121(6):1068-1100. https://doi.org/10.1002/nme.6257
58. Li C, Borja RI, Regueiro RA. Dynamics of porous media at finite strain. *Comput Methods Appl Mech Eng*. 2004;193(36-38):3837-3870.
59. Navas P, Sanavia L, López-Querol S, Rena CY. u-w formulation for dynamic problems in large deformation regime solved through an implicit meshfree scheme. *Comput Mech*. 2018;62:745-760. https://doi.org/10.1007/s00466-017-1524-y

How to cite this article: Molinos M, Martín Stickle M, Navas P, Yagüe Á, Manzanal D, Pastor M. Toward a local *maximum-entropy* material point method at finite strain within a B-free approach. *Int J Numer Methods Eng*. 2021;1–32. https://doi.org/10.1002/nme.6765

APPENDIX A. DETAILED DESCRIPTION OF THE RELATED CONSISTENT LINEARIZATION FOR THE NONLINEAR RESIDUAL

This appendix contains a detailed description of the linearization process briefly introduced in Section 3.3. The derivation is algebraically tedious. As such, a number of intermediate results as well as the following lemmas are established for the later use.

Lemma 1. *The derivative of the inverse any nonsingular tensor* $\mathbf{A}$ *can be expressed as* $\delta\mathbf{A}^{-1} = -\mathbf{A}^{-1}\ \delta\mathbf{A}\ \mathbf{A}^{-1}$.

Proof. Consider the relation $\mathbf{A}^{-1}\mathbf{A} = \mathbf{I}$ as starting point:

$$\begin{aligned}\delta\mathbf{A}^{-1}\ \mathbf{A} + \mathbf{A}^{-1}\ \delta\mathbf{A} &= \delta\mathbf{I} = 0,\\ \delta\mathbf{A}^{-1}\ \mathbf{A} &= -\mathbf{A}^{-1}\ \delta\mathbf{A},\\ \delta\mathbf{A}^{-1} &= -\mathbf{A}^{-1}\ \delta\mathbf{A}\ \mathbf{A}^{-1}.\end{aligned}$$

■

Lemma 2. *The inverse of a symmetric tensor* $\mathbf{A}$ *is the symmetric tensor* $\mathbf{A}^{-1} = \mathbf{A}^{-T}$.

Proof. By application of the Hamilton–Cayley theorem:

$$\mathbf{A}^{-1} = \frac{1}{I_3}(\mathbf{A}^2 - I_1\mathbf{A} + I_2\mathbf{I}).$$

The tensor $\mathbf{A}^{-1}$ can be constructed as a combination of the symmetric tensor $\mathbf{A}$ and its invariants $(I_3,\ I_2,\ I_1)$, therefore, the resulting tensor *must be* symmetric. ■

Here some useful intermediate linearization are presented to simplify further developments. Firstly, the acceleration term is linearized considering the Newmark scheme expressed in the Equation (18):

$$\frac{d}{d\epsilon}\Big|_{\epsilon=0}\ \mathbf{a}(\varphi_{n+1} + \epsilon D\varphi) = \alpha_1 D\varphi. \tag{A1}$$

In second place, the deformation gradient tensor $\mathbf{F}$ is linearized as:

$$\frac{d}{d\epsilon}\Big|_{\epsilon=0}\ \mathbf{F}(\varphi_{n+1} + \epsilon D\varphi) = GRAD(D\varphi). \tag{A2}$$

In third place, the determinant of the deformation gradient tensor I_3, also named as J, is linearized by the application of the Hamilton–Cayley theorem:

$$\frac{d}{d\epsilon}\Big|_{\epsilon=0}\ I_3(\varphi_{n+1} + \epsilon D\varphi) = \frac{\partial I_3}{\partial\mathbf{F}} : \frac{d}{d\epsilon}\Big|_{\epsilon=0}\ \mathbf{F}(\varphi_{n+1} + \epsilon D\varphi) = (\mathbf{F}^2 - I_1\mathbf{F} + I_2\mathbf{I})^T : GRAD(D\varphi) = I_3\mathbf{F}^{-T} : GRAD(D\varphi). \tag{A3}$$

In fourth place, the right Cauchy–Green tensor $\mathbf{C}$ herein linearized:

$$\frac{d}{d\epsilon}\Big|_{\epsilon=0}\ \mathbf{C}(\varphi_{n+1} + \epsilon D\varphi) = GRAD(D\varphi)^T\mathbf{F}_{n+1} + \mathbf{F}_{n+1}^T GRAD(D\varphi). \tag{A4}$$

Finally, the second Piola–Kirchhoff stress tensor $\mathbf{S}$ linearization reads:

$$\frac{d}{d\epsilon}\Big|_{\epsilon=0}\ \mathbf{S}(\varphi_{n+1} + \epsilon D\varphi) = \frac{\partial\mathbf{S}}{\partial\mathbf{C}} : \frac{d}{d\epsilon}\Big|_{\epsilon=0}\ \mathbf{C}(\varphi_{n+1} + \epsilon D\varphi) = 2\ \frac{\partial\mathbf{S}}{\partial\mathbf{C}} : \mathbf{F}_{n+1}^T GRAD(D\varphi) = \mathbb{C} : \mathbf{F}_{n+1}^T GRAD(D\varphi). \tag{A5}$$

Observe that the symmetry of $\mathbb{C}$ has been taken in to account to reach the final expression. Once these auxiliary expressions have been linearized, at this point, let us introduce the following tensorial equality proposed by Planas et al.:[23]

$$[\mathbb{T} : (\delta\mathbf{a} \otimes \mathbf{b})]\mathbf{v} = \mathbb{T}\{\mathbf{v}, \mathbf{b}\}\ \delta\mathbf{a} \tag{A6}$$

for any vectors $\mathbf{v}, \mathbf{b}, \delta\mathbf{a} \in \mathbb{R}^{n_{dim}}$ and any fourth-order tensor $\mathbb{T} : \square$. After these definitions, the linearization process for the functional $\mathcal{L}(\varphi_{n+1}, \psi)$ yields:

$$\begin{aligned}
D\mathcal{L}(\varphi_{n+1}, \psi)D\varphi &= \left.\frac{d}{d\epsilon}\right|_{\epsilon=0} \mathcal{L}(\varphi_{n+1}, \psi) \\
&= \left.\frac{d}{d\epsilon}\right|_{\epsilon=0} \int_{\mathcal{B}_0} \rho_0\ \mathbf{a}(\varphi_{n+1} + \epsilon D\varphi) \cdot \psi\ dV - \int_{\mathcal{B}_0} \mathbf{F}(\varphi_{n+1} + \epsilon D\varphi)\ \mathbf{S}(\varphi_{n+1} + \epsilon D\varphi) : GRAD(\psi)\ dV \\
&\overset{a}{=} \int_{\mathcal{B}_0} \rho_0\ \left.\frac{d}{d\epsilon}\right|_{\epsilon=0} \mathbf{a}(\varphi + \epsilon D\varphi)_{n+1} \cdot \psi\ dV - \int_{\mathcal{B}_0} \left.\frac{d}{d\epsilon}\right|_{\epsilon=0} \mathbf{F}(\varphi + \epsilon D\varphi)_{n+1}\ \mathbf{S}_{n+1} : GRAD(\psi)\ dV - \\
&\int_{\mathcal{B}_0} \mathbf{F}_{n+1}\ \left.\frac{d}{d\epsilon}\right|_{\epsilon=0} \mathbf{S}(\varphi + \epsilon D\varphi)_{n+1} : GRAD(\psi)\ dV \\
&\overset{b}{=} \int_{\mathcal{B}_0} \rho_0\ \alpha_1 D\varphi \cdot \psi\ dV - \int_{\mathcal{B}_0} GRAD(D\varphi)\ \mathbf{S}_{n+1} : GRAD(\psi)\ dV - \\
&\int_{\mathcal{B}_0} \mathbf{F}_{n+1}\ \left[\mathbb{C} : \mathbf{F}_{n+1}^T GRAD(D\varphi)\right] : GRAD(\psi)\ dV.
\end{aligned} \tag{A7}$$

[a] ϵ derivative can entered into the integral since we are in the reference configuration
[b] Introducing expressions A1, A2, and A5

At this point of the derivation, the spatial discretization described in Section 3.2 is introduced. Hereinafter, in aims of clarity in the notation, the Einstein's summation convention for repeated index has been adopted, and each term of the functional derivative is developed separately. The first term is easily identified as a mass matrix:

$$\begin{aligned}
\int_{\mathcal{B}_0} \rho_0\ \alpha_1 D\varphi \cdot \psi\ dV &= \alpha_1 \int_{\mathcal{B}_0} \rho_0\ D\varphi^J_{n+1} N(\mathbf{x})^J\ \cdot \psi^I N(\mathbf{x})^I\ dV \\
&= \alpha_1 \int_{\mathcal{B}_0} \rho_0\ D\varphi^J_{n+1} N(\mathbf{x})^J\ \cdot \psi^I N(\mathbf{x})^I dV \\
&= \psi^I \cdot \alpha_1 \int_{\mathcal{B}_0} N(\mathbf{x})^I\ \rho_0\ N(\mathbf{x})^J dV\ D\varphi^J_{n+1}.
\end{aligned} \tag{A8}$$

The second term corresponds to the geometrical contribution of the tangent stiffness

$$\begin{aligned}
\int_{\mathcal{B}_0} GRAD(D\varphi)\ \mathbf{S}_{n+1} : GRAD(\psi)\ dV &= \int_{\mathcal{B}_0} \left(D\varphi^I_{n+1} \otimes GRAD(N(\mathbf{x})^I)\right)\ \mathbf{S}_{n+1} : \left(\psi^J \otimes GRAD(N(\mathbf{x})^J)\right) dV \\
&\overset{a}{=} \int_{\mathcal{B}_0} \left(D\varphi^I_{n+1} \otimes \mathbf{S}_{n+1} GRAD(N(\mathbf{x})^I)\right)\ : \left(\psi^J \otimes GRAD(N(\mathbf{x})^J)\right) dV \\
&= \int_{\mathcal{B}_0} \mathbf{S}_{n+1} : \left(GRAD(N(\mathbf{x})^I)\ \otimes GRAD(N(\mathbf{x})^J)\right)\ \left(D\varphi^I_{n+1} \cdot \psi^J\right) dV.
\end{aligned} \tag{A9}$$

[a] Using the symmetry of $\mathbf{S}$.

The third term corresponds to the material contribution of the tangent stiffness.

$$
\begin{aligned}
&\int_{\mathcal{B}_0} \mathbf{F}_{n+1}\ \left[\mathbb{C} : \mathbf{F}_{n+1}^T GRAD(D\varphi)\right] : GRAD(\psi)\, dV \ = \int_{\mathcal{B}_0} \mathbf{F}_{n+1}^T GRAD(\psi)\ :\ \left[\mathbb{C} : GRAD(D\varphi)^T \mathbf{F}_{n+1}\right]\ dV \\
&= \int_{\mathcal{B}_0} \mathbf{F}_{n+1}^T \left(\psi^I \otimes GRAD(N(\mathbf{x})^I)\right)\ :\ \left[\mathbb{C} : \left(GRAD(N(\mathbf{x})^J)\ \otimes D\varphi_{n+1}^J\right)\mathbf{F}_{n+1}\right]\ dV \\
&= \int_{\mathcal{B}_0} \left(\mathbf{F}_{n+1}^T\psi^I \otimes GRAD(N(\mathbf{x})^I)\right)\ :\ \left[\mathbb{C} : \left(GRAD(N(\mathbf{x})^J)\ \otimes \mathbf{F}_{n+1}^T D\varphi_{n+1}^J\right)\right]\ dV \\
&= \int_{\mathcal{B}_0} \left(\mathbf{F}_{n+1}^T\psi^I \otimes GRAD(N(\mathbf{x})^I)\right)\ :\ \left[\mathbb{C} : \left(\mathbf{F}_{n+1}^T D\varphi_{n+1}^J \otimes GRAD(N(\mathbf{x})^J)\ \right)\right]\ dV \\
&= \int_{\mathcal{B}_0} \mathbf{F}_{n+1}^T\psi^I \cdot \left[\mathbb{C} : \left(\mathbf{F}_{n+1}^T D\varphi_{n+1}^J \otimes GRAD(N(\mathbf{x})^J)\ \right)\right]\ GRAD(N(\mathbf{x})^I) dV \\
&\overset{a}{=} \int_{\mathcal{B}_0} \mathbf{F}_{n+1}^T\psi^I\ \cdot \mathbb{C}\{GRAD(N(\mathbf{x})^I), GRAD(N(\mathbf{x})^I)\}\ \mathbf{F}_{n+1}^T D\varphi_{n+1}^J\ dV \\
&= \psi^I \cdot \int_{\mathcal{B}_0} \mathbf{F}_{n+1}\ \mathbb{C}\{GRAD(N(\mathbf{x})^I), GRAD(N(\mathbf{x})^I)\}\ \mathbf{F}_{n+1}^T\ dV\ D\varphi_{n+1}^J.
\end{aligned}
\tag{A10}
$$

[a] Exploiting **B**-free relation (Equation A6) and considering $\mathbf{v} = GRAD(N(\mathbf{x}))^J$, $\mathbf{b} = GRAD(N(\mathbf{x}))^I$, $\delta\mathbf{a} = \mathbf{F}_{n+1} D\varphi_{n+1}^I$, and $\mathbb{T} : \square = \mathbb{C} : \square$.

Finally, introducing Equations (A8), (A9), and (A10) in Equation (A7), and taking in to account that $\forall\ \psi^I \in \mathcal{W}^h$, the final expression for the tangent matrix under the B-free approach is obtained:

$$
\begin{aligned}
D\mathcal{L}(\varphi_{n+1},)^{IJ} D\varphi_{n+1}^J = \alpha_1 &\int_{\mathcal{B}_0} N(\mathbf{x})^I\ \rho_0\ N(\mathbf{x})^J dV\ D\varphi_{n+1}^J \\
&- \int_{\mathcal{B}_0} \mathbf{S}_{n+1}\ :\ (GRAD(N(\mathbf{x})^I)\ \otimes GRAD(N(\mathbf{x})^J))\mathbf{I}\ dV\ D\varphi_{n+1}^J \\
&- \int_{\mathcal{B}_0} \mathbf{F}_{n+1}\ \mathbb{C}\{GRAD(N(\mathbf{x})^I), GRAD(N(\mathbf{x})^J)\}\ \mathbf{F}_{n+1}^T\ dV\ D\varphi_{n+1}^J.
\end{aligned}
\tag{A11}
$$

APPENDIX B. DETAILED FACTORIZATION PROCESS

This appendix contains a detailed description of the factorization process for two kinds of well-known hyperelastic constitutive models, the St. Venant–Kirchhoff material B.2, and the Ciarlet's[26] Neo-Hookean material B.1.

B.1 Factorization of the Neo-Hookean material model

A general definition of this model is given by the equation:

$$
W^e(\mathbf{C}) = g(J) + \frac{1}{2} G(I_C - 3), \tag{B1}
$$

where $g(J)$ is a function which contains the compressible part, which changes in different constitutive laws depending on the authors. According to Ciarlet:[26]

$$
g(J) = c(J^2 - 1) - d \ln J - G \ln J \quad \text{with} \quad c > 0, d > 0, \tag{B2}
$$

c and d are constant that depends of Λ. Finally, G and Λ are the well-known Lamé parameters. From the derivation of the energy with respect to the own right Cauchy–Green tensor, it can be obtained the second Piola–Kirchhoff stress tensor:

$$
\mathbf{S} = 2\ \frac{\partial W^e(\mathbf{C})}{\partial \mathbf{C}} = \frac{\Lambda}{2}\ (J^2 - 1)\ \mathbf{C}^{-1} + G\ (\mathbf{I} - \mathbf{C}^{-1}). \tag{B3}
$$

Finally, $\mathbb{C} : \square$ is the symmetric fourth-order tensor, known as the Lagrangian or material elasticity tensor:

$$
\mathbb{C} = 2\frac{\partial \mathbf{S}}{\partial \mathbf{C}} = \Lambda J^2 \mathbf{C}^{-1} \otimes \mathbf{C}^{-1} + (\Lambda\ (J^2 - 1) - 2G)\frac{\partial \mathbf{C}^{-1}}{\partial \mathbf{C}}. \tag{B4}
$$

From the derivation of Equation (A10) we got the following expression:

$$[\mathbb{C} : (\mathbf{F}^T_{n+1} D\varphi^J_{n+1} \otimes GRAD(N(\mathbf{x})^J))]\ GRAD(N(\mathbf{x})^I).$$

According to Planas et al.[23] we pretend to factoring out the variation of the displacement, $\mathbf{F}^T_{n+1} D\varphi^J_{n+1}$, in the foregoing expression, a new tensor-valued linear operation is found in Equation (A6). Doing the following change of variables to simplify the manipulation:

$$\mathbf{v} = GRAD(N(\mathbf{x}))^J, \quad \mathbf{b} = GRAD(N(\mathbf{x}))^I, \quad \delta\mathbf{a} = \mathbf{F}_{n+1} D\varphi^I_{n+1}, \quad \text{and} \quad \mathbb{T} : \square = \mathbb{C} : \square.$$

For the particular case of the Neo-Hookean the factorization process in the following:

$$\begin{aligned}
[\mathbb{T} : (\delta\mathbf{a} \otimes \mathbf{b})]\,\mathbf{v} &=^{a\,b\,c} \left[\Lambda J^2 \left(\mathbf{C}^{-1} : (\delta\mathbf{a} \otimes \mathbf{b})\right) \mathbf{C}^{-1} - \left(\frac{\Lambda}{2}\left(J^2 - 1\right) - G\right)\left(\mathbf{C}^{-1}\delta\mathbf{a} \otimes \mathbf{C}^{-T}\mathbf{b} + \mathbf{C}^{-1}\mathbf{b} \otimes \mathbf{C}^{-T}\delta\mathbf{a}\right)\right]\mathbf{v} \\
&=^{d} \Lambda J^2 \left(\delta\mathbf{a} \cdot \mathbf{C}^{-1}\mathbf{b}\right)\mathbf{C}^{-1}\mathbf{v} - \left(\frac{\Lambda}{2}\left(J^2 - 1\right) - G\right)\left(\mathbf{v} \cdot \mathbf{C}^{-1}\mathbf{b}\right)\mathbf{C}^{-1}\delta\mathbf{a} - \\
&\quad \left(\frac{\Lambda}{2}(J^2 - 1) - G\right)\left(\mathbf{C}^{-1}\delta\mathbf{a} \cdot \mathbf{v}\right)\mathbf{C}^{-1}\mathbf{b} \\
&=^{e} \Lambda J^2 \left(\mathbf{C}^{-1}\mathbf{v} \otimes \mathbf{C}^{-1}\mathbf{b}\right)\delta\mathbf{a} - \left(\frac{\Lambda}{2}\left(J^2 - 1\right) - G\right)\left(\mathbf{C}^{-1}\mathbf{b} \cdot \mathbf{v}\right)\mathbf{C}^{-1}\delta\mathbf{a} - \\
&\quad \left(\frac{\Lambda}{2}\left(J^2 - 1\right) - G\right)\left(\mathbf{C}^{-1}\mathbf{b} \otimes \mathbf{C}^{-1}\mathbf{v}\right)\delta\mathbf{a} \\
&= \mathbb{T}\{\mathbf{v}, \mathbf{b}\}\ \delta\mathbf{a}
\end{aligned} \tag{B5}$$

[a] Particularizing with Equation (B4).
[b] Applying the property $(\mathbf{A} \otimes \mathbf{B})\,\mathbf{C} = (\mathbf{B} : \mathbf{C})\,\mathbf{A}$.
[c] Applying Lemma 1 together with Equation (A4).
[d] Applying Lemma 2.
[e] Applying the property $(\mathbf{a} \otimes \mathbf{b})\mathbf{c} = (\mathbf{b} \cdot \mathbf{c})\mathbf{a} = (\mathbf{c} \cdot \mathbf{b})\mathbf{a}$.

Finally, after undoing the change of variable, the final expression, yields as:

$$\begin{aligned}
&\mathbb{C}\{GRAD(N(\mathbf{x}))^I, GRAD(N(\mathbf{x}))^J\}\ \mathbf{F}_{n+1} D\varphi^I_{n+1} \\
&\quad = \Lambda J^2 (\mathbf{C}^{-1} GRAD(N(\mathbf{x}))^I \otimes \mathbf{C}^{-1} GRAD(N(\mathbf{x}))^J)\mathbf{F}_{n+1} D\varphi^I_{n+1} \\
&\qquad - \left(\frac{\Lambda}{2}(J^2 - 1) - G\right)(\mathbf{C}^{-1} GRAD(N(\mathbf{x}))^J \cdot GRAD(N(\mathbf{x}))^J)\mathbf{C}^{-1}\mathbf{F}_{n+1} D\varphi^I_{n+1} \\
&\qquad - \left(\frac{\Lambda}{2}(J^2 - 1) - G\right)(\mathbf{C}^{-1} GRAD(N(\mathbf{x}))^J \otimes \mathbf{C}^{-1} GRAD(N(\mathbf{x}))^I)\mathbf{F}_{n+1} D\varphi^I_{n+1}.
\end{aligned} \tag{B6}$$

B.2 Factorization of the St. Venant–Kirchhoff Material

A general definition of this model is given by the equation:

$$W^e(\mathbf{E}) = \frac{1}{2}\Lambda tr(\mathbf{E})^2 + G\mathbf{E} : \mathbf{E}, \tag{B7}$$

where G and Λ are the well-known Lamé parameters. From the derivation of the energy with respect to the own right Cauchy–Green tensor, it can be obtained the second Piola–Kirchhoff stress tensor:

$$\mathbf{S} = \frac{\partial W^e(\mathbf{E})}{\partial \mathbf{E}} = \Lambda\ tr(\mathbf{E})\mathbf{I} + 2G\mathbf{E}. \tag{B8}$$

Finally, $\mathbb{C} : \square$ is the symmetric fourth-order tensor, known as the Lagrangian or material elasticity tensor is obtained as:

$$\mathbb{C} = \frac{\partial \mathbf{S}}{\partial \mathbf{E}} = \Lambda \mathbf{I} \otimes \mathbf{I} + G\frac{\partial \mathbf{E}}{\partial \mathbf{E}}. \tag{B9}$$

From the derivation of Equation (A10) we got the following expression,

$$[\mathbb{C} : (\mathbf{F}^T_{n+1} D\varphi^J_{n+1} \otimes GRAD(N(\mathbf{x})^J))]\ GRAD(N(\mathbf{x})^I).$$

According to Planas et al.[23] we pretend to factoring out the variation of the displacement, $\mathbf{F}_{n+1}^{T} D\varphi_{n+1}^{J}$, in the foregoing expression, a new tensor-valued linear operation is found in Equation (A6). Doing the following change of variables to simplify the manipulation:

$$\mathbf{v} = GRAD(N(\mathbf{x}))^{J}, \quad \mathbf{b} = GRAD(N(\mathbf{x}))^{I}, \quad \delta\mathbf{a} = \mathbf{F}_{n+1} D\varphi_{n+1}^{I}, \quad \text{and} \quad \mathbb{T} : \square = \mathbb{C} : \square.$$

For the particular case of the St. Venant–Kirchhoff, the material tangent density tensor has the following expression:

$$\begin{aligned}
[\mathbb{T} : (\delta\mathbf{a} \otimes \mathbf{b})]\,\mathbf{v} &=^{a\,b\,c} [\Lambda\,(\mathbf{I} : (\delta\mathbf{a} \otimes \mathbf{b}))\,\mathbf{I} + G(\mathbf{I}\delta\mathbf{a} \otimes \mathbf{I}\mathbf{b} + \mathbf{I}\mathbf{b} \otimes \mathbf{I}\delta\mathbf{a})]\,\mathbf{v} \\
&= \Lambda\,(\delta\mathbf{a} \cdot \mathbf{b})\,\mathbf{v} + G(\delta\mathbf{a} \otimes \mathbf{b})\mathbf{v} + G(\mathbf{b} \otimes \delta\mathbf{a})\mathbf{v} \\
&=^{d} \Lambda\,(\mathbf{v} \otimes \mathbf{b})\,\delta\mathbf{a} + G(\mathbf{v} \cdot \mathbf{b})\delta\mathbf{a} + G(\mathbf{b} \otimes \mathbf{v})\delta\mathbf{a} \\
&= \mathbb{T}\{\mathbf{v}, \mathbf{b}\}\;\delta\mathbf{a}.
\end{aligned} \tag{B10}$$

[a] Particularizing with Equation (B4).
[b] Applying the property $(\mathbf{A} \otimes \mathbf{B})\,\mathbf{C} = (\mathbf{B} : \mathbf{C})\,\mathbf{A}$.
[c] Applying the well-known definition $\left(\frac{\partial \mathbf{A}}{\partial \mathbf{A}}\right) = \frac{1}{2}\left(\mathbf{I}_{il}\mathbf{I}_{mk} + \mathbf{I}_{im}\mathbf{I}_{lk}\right)$.
[d] Applying the property $(\mathbf{a} \otimes \mathbf{b})\mathbf{c} = (\mathbf{b} \cdot \mathbf{c})\mathbf{a} = (\mathbf{c} \cdot \mathbf{b})\mathbf{a}$.

Finally, after undoing the change of variable, the final expression, yields as:

$$\begin{aligned}
\mathbb{C}\{GRAD(N(\mathbf{x}))^{I}, GRAD(N(\mathbf{x}))^{J}\}\;\mathbf{F}_{n+1} D\varphi_{n+1}^{I} &= \Lambda(GRAD(N(\mathbf{x}))^{I} \otimes GRAD(N(\mathbf{x}))^{J})\mathbf{F}_{n+1} D\varphi_{n+1}^{I} \\
&+ G(GRAD(N(\mathbf{x}))^{I} \cdot GRAD(N(\mathbf{x}))^{J})\mathbf{F}_{n+1} D\varphi_{n+1}^{I} \\
&+ G(GRAD(N(\mathbf{x}))^{J} \otimes GRAD(N(\mathbf{x}))^{I})\mathbf{F}_{n+1} D\varphi_{n+1}^{I}.
\end{aligned} \tag{B11}$$

APPENDIX C. PSEUDO-CODES FOR HYPERELASTIC BOUNDARY VALUE PROBLEM

The following algorithms summarize the numerical realization of the presented **B**-free updated-Lagrangian material point method.

Algorithm 1. Incremental Newmark-β algorithm

1: Generate Nodal Mask.
2: Compute Nodal Effective Matrix:

$$\tilde{\mathbf{M}}^{IJ} = (1 - \epsilon)\,\mathbf{M}^{IJ} + \epsilon\,\bar{\mathbf{M}}^{IJ}$$

3: Compute Nodal Velocity and Acceleration fields solving:

$$\tilde{\mathbf{M}}^{IJ}\,\mathbf{v}_n^{J} = \sum_{p\,\in\,\mathcal{C}} N_n^{Ip}\,m^{p}\,\mathbf{v}_n^{p} \quad \text{and} \quad \tilde{\mathbf{M}}^{IJ}\mathbf{a}_n^{J} = \sum_{p\,\in\,\mathcal{C}} N_n^{Ip}\,m^{p}\,\mathbf{a}_n^{p}$$

4: Impose the Dirichlet boundary conditions.
5: Compute nodal displacement increments $\Delta\varphi^{I}$ by assembly and iterative solution (Algorithm 2)
6: Update particles quantities:

$$\begin{aligned}
\mathbf{a}_{n+1}^{p} &= \mathbf{a}_n^{p} + \sum_{I\,\in\,\mathcal{A}^{p}} N_n^{Ip} \cdot (\alpha_1\,\Delta\varphi^{I} - \alpha_2\,\mathbf{v}_n^{I} - (\alpha_3 + 1)\,\mathbf{a}_n^{I}), \\
\mathbf{v}_{n+1}^{p} &= \mathbf{v}_n^{p} + \sum_{I\,\in\,\mathcal{A}^{p}} N_n^{Ip} \cdot \left(\alpha_4\,\Delta\varphi^{I} + (\alpha_5 - 1)\,\mathbf{v}_n^{I} + \alpha_6\,\mathbf{a}_n^{I}\right), \\
\mathbf{x}_{n+1}^{p} &= \mathbf{x}_n^{p} + \sum_{I\,\in\,\mathcal{A}^{p}} N_n^{Ip}\,\Delta\varphi^{I}.
\end{aligned}$$

7: Update the connectivity $\mathcal{A}^{p}$ for each particle (Algorithm 3).
8: Reset nodal values and updating solution $n + 1 \rightarrow n$:

$$\mathbf{a}_n^{p} = \mathbf{a}_{n+1}^{p}, \quad \mathbf{v}_n^{p} = \mathbf{v}_{n+1}^{p}, \quad \mathbf{x}_n^{p} = \mathbf{x}_{n+1}^{p}, \quad \text{and} \quad \mathbf{F}_n^{p} = \mathbf{F}_{n+1}^{p}$$

Algorithm 2. Assembly and solver

Input
- $\mathcal{A}^p$ List of neighborhood nodes for each particle p
- V^p Reference volume for each particle p
- $GRAD(\square)$ Gradient operator in the reference configuration, $\mathcal{B}_0$
- $GRAD_n(\square)$ Gradient operator in the n configuration, $\mathcal{B}_n$
- $\mathbf{F}^p_n,\ \mathbf{F}^p_{n+1}$ Deformation gradient at the instants n and $n+1$
- $\mathbb{C}_{mat}\{\square,\square\}$ Factorised material tangent stiffness

while ${}^i\|\mathcal{L}_I\|_{\text{Relative}} >$ Tolerance **do**

Update local state from n to n + 1:
for p to n_p **do**
Compute incremental deformation gradient: $\Delta\mathbf{F}^p_{n\to n+1} = \mathbf{I} + \sum_{I\in\mathcal{A}^p} {}^i\left[\Delta\varphi^I\right] \otimes GRAD_n(N^{Ip})$
Compute total deformation gradient: $\mathbf{F}^p_{n+1} = \Delta\mathbf{F}^p_{n\to n+1}\mathbf{F}^p_n$
Compute Second Piola-Kirchhoff tensor: $\mathbf{S}^p = \mathbf{S}(\mathbf{F}^p_{n+1})$
end for

Compute nodal residual ${}^i\left[\mathcal{L}^I_{n+1}\right]$:
for I to n_I **do**
${}^i\left[\mathcal{L}^I_{n+1}\right] \leftarrow {}^i\left[\mathcal{L}^I_{n+1}\right] + \left[\tilde{\mathbf{M}}^{IJ}\right]\cdot(\alpha_1\,{}^i\left[\Delta\varphi^J\right] - \alpha_2\left[\mathbf{v}^J_n\right] - \alpha_3\left[\mathbf{a}^J_n\right])$
end for
for p to n_p **do**
for $I \in \mathcal{A}^p$ **do**
${}^i\left[\mathcal{L}^I_{n+1}\right] \leftarrow {}^i\left[\mathcal{L}^I_{n+1}\right] + \mathbf{F}^p_{n+1}\mathbf{S}^p\, GRAD(N^{Ip})\, V^p - N^{Ip}\,\mathbf{b}^p\, m^p$
end for
end for

Assemble the non-linear tangent matrix ${}^i\left[\mathbf{K}^I_{n+1}\right]$:
for p to n_p **do**
for $I \in \mathcal{A}^p$ **do**
for $J \in \mathcal{A}^p$ **do**
${}^i\left[\mathbf{K}^I_{n+1}\right] \leftarrow {}^i\left[\mathbf{K}^I_{n+1}\right] + {}^i\left[\mathbf{F}^p_{n+1}\mathbb{C}_{mat}\{GRAD(N^{Ip}), GRAD(N^{Jp})\}\mathbf{F}^{p,T}_{n+1}\right]V^p$
${}^i\left[\mathbf{K}^I_{n+1}\right] \leftarrow {}^i\left[\mathbf{K}^I_{n+1}\right] + {}^i\left[\mathbf{S}^p\cdot\left(GRAD(N^{Ip})\otimes GRAD(N^{Jp})\right)\mathbf{I}\right]V^p$
end for
end for
end for
for I to n_I **do**
for J to n_J **do**
${}^i\left[\mathbf{K}^I_{n+1}\right] \leftarrow {}^i\left[\mathbf{K}^I_{n+1}\right] + \alpha_1\left[\tilde{\mathbf{M}}^{IJ}\right]$
end for
end for

Newton-Raphson step:
${}^{i+1}\left[\Delta\varphi^I\right] = {}^i\left[\Delta\varphi^I\right] - {}^i\left[\mathbf{K}^{IJ}_{n+1}\right]^{-1}\cdot {}^i\left[\mathcal{L}^J_{n+1}\right]$

Check the number of iterations:
if $i >$ Max number of iterations **then**
Failure
end if

end while

Algorithm 3. Reconstruction of the particle nodal connectivity

Input

- $\mathcal{A}^p{}_{old}$ Old connectivity list for each particle p
- I_0 Closest node for each particle
- $I_{Nodes}(I)$ Returns the neighborhood of the node I
- β *Thermalization* parameter
- TOL_0 Shape function decay tolerance[6]. Typical value 10^{-6}
- $d(x, y)$ Computes the Euclidean distance between two points x and y.

Output

- $\mathcal{A}^p{}_{new}$ Updated the connectivity list for each particle p

for p to N_p **do**

$R = \sqrt{-\log(TOL_0)/\beta}$

$I_0 = \text{Find } I \in \mathcal{A}^p_{old} \mid \min d(x^p, x^I)$

$\mathcal{A}^{I,n} = I_{Nodes}(I_0)$

$\mathcal{A}^p_{new} = \text{Find } \mathbf{x}^I \in \mathcal{A}^{I,n} \mid \sqrt{(\mathbf{x}^p - \mathbf{x}^I) \cdot (\mathbf{x}^p - \mathbf{x}^I)} < h\sqrt{-\log(TOL_0)/\widehat{\gamma}}$

end for